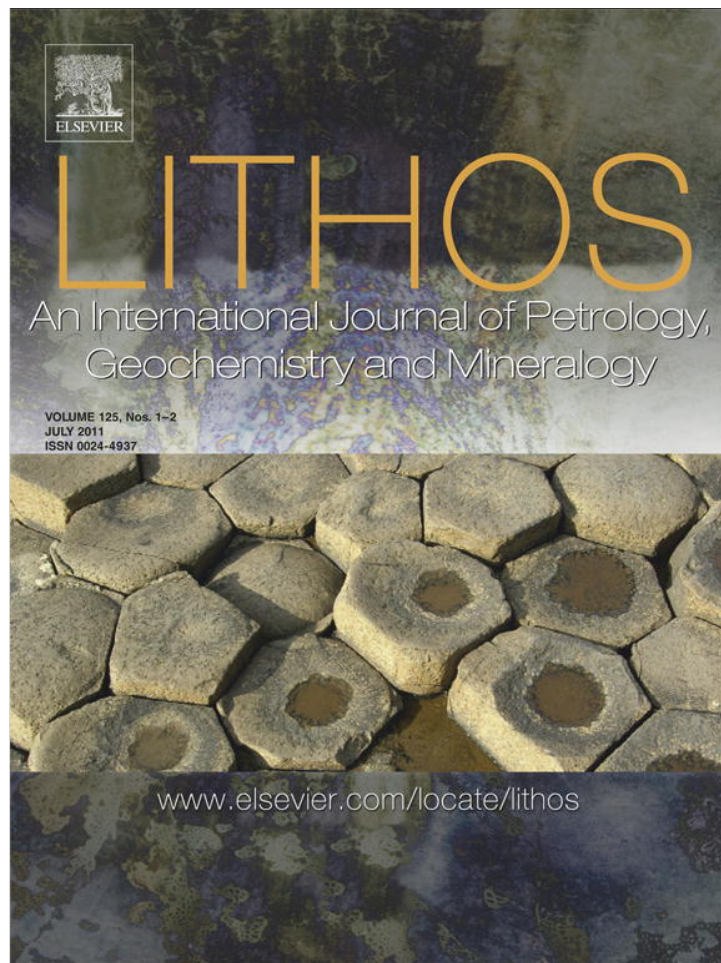


Provided for non-commercial research and education use.
Not for reproduction, distribution or commercial use.



This article appeared in a journal published by Elsevier. The attached copy is furnished to the author for internal non-commercial research and education use, including for instruction at the authors institution and sharing with colleagues.

Other uses, including reproduction and distribution, or selling or licensing copies, or posting to personal, institutional or third party websites are prohibited.

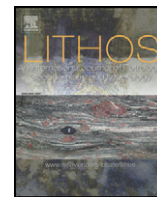
In most cases authors are permitted to post their version of the article (e.g. in Word or Tex form) to their personal website or institutional repository. Authors requiring further information regarding Elsevier's archiving and manuscript policies are encouraged to visit:

<http://www.elsevier.com/copyright>



Contents lists available at ScienceDirect

Lithos

journal homepage: www.elsevier.com/locate/lithos

Mafic and felsic magma interaction during the construction of high-K calc-alkaline plutons within a metacratonic passive margin: The Early Permian Guyang batholith from the northern North China Craton

Xiaohui Zhang^{a,*}, Qian Mao^a, Hongfu Zhang^a, Mingguo Zhai^a, Yueheng Yang^a, Zhaochu Hu^b

^a State Key Laboratory of Lithospheric Evolution, Institute of Geology and Geophysics, Chinese Academy of Sciences, Beijing 100029, China

^b State Key Laboratory of Geological Processes and Mineral Resources, China University of Geosciences, Wuhan 430074, China

ARTICLE INFO

Article history:

Received 15 September 2010

Accepted 4 March 2011

Available online 11 March 2011

Keywords:

Early Permian

Magma mixing

High-K calc-alkaline batholith

Post-collisional

Metacraton

North China Craton

ABSTRACT

Zircon U–Pb and hornblende $^{40}\text{Ar}/^{39}\text{Ar}$ dating document an Early Permian emplacement time for the Hercynian Guyang batholith from the northern margin of the North China Craton (NCC), with a variety of lithologies including: gabbro–gabbroic diorite–leuconorite, diorite and granodiorite, microgranular magmatic enclaves (MME), mafic dyke and monzogranite. Field relations, petrological, elemental, whole-rock Sr–Nd and zircon Hf isotopic data show that (1) the gabbros and gabbroic diorites exhibit strong enrichment of large ion lithophile element (LILE) and light rare earth element (LREE), depletion in high field strength element (HFSE), and have moderately enriched isotopic compositions with $^{87}\text{Sr}/^{86}\text{Sr}_i$ ranging from 0.7050 to 0.7053, $\epsilon_{\text{Nd}}(t)$ from -8.08 to -10.2 and zircon $\epsilon_{\text{Hf}}(t)$ from -6.7 to -12.0 ; while the leuconorites are characterized by low REE contents, conspicuous positive Eu anomaly and comparable Sr–Nd compositions to gabbroic rocks. These features suggest that they may represent complementary products from a parental magma derived from a subduction-related metasomatized sub-continental lithospheric mantle (SCLM) source; (2) the monzogranites range from 74.3 to 75.6% SiO_2 , with high Sr–Ba abundances and elevated Sr/Y and La/Yb ratios. Such high-silica adakitic affinity, plus their indistinguishable isotopic compositions from the mafic ones ($^{87}\text{Sr}/^{86}\text{Sr}_i = 0.7053$ to 0.7055, $\epsilon_{\text{Nd}}(t) = -10.5$ to -11.3 , zircon $\epsilon_{\text{Hf}}(t) = -8.5$ to -11.8), indicates a felsic parental magma from partial melting of mixed protoliths composed of newly underplated mafic lower crustal and ancient mafic lower crustal materials; (3) the diorites and granodiorites contain abundant MME and display various scales of petrologic textures indicative of magma mixing. They also have intermediate geochemical compositions between gabbroic diorite and granite. Combined with their evolved isotopic compositions ($^{87}\text{Sr}/^{86}\text{Sr}_i = 0.7050$ to 0.7064, $\epsilon_{\text{Nd}}(t) = -8.36$ to -13.9 , zircon $\epsilon_{\text{Hf}}(t) = -7.9$ to -15.5), they are inferred to be formed by mixing between SCLM-derived mafic magma and crustal-derived felsic magma; (4) the MME show igneous texture with SiO_2 contents between 49.2 and 54.7%. Their trace elements and evolved isotopic character ($^{87}\text{Sr}/^{86}\text{Sr}_i = 0.7049$ –0.7056, $\epsilon_{\text{Nd}}(t) = -8.48$ to -10.1 ; zircon $\epsilon_{\text{Hf}}(t) = -8.8$ to -14.7) indicate that they represent mafic magmas derived from the enriched SCLM and hybridized by diffusion and mechanical mixing with their host granitoids; and (5) the late-stage mafic dykes are gabbroic dioritic to dioritic in composition, with enrichment in LILE and LREE relative to HFSE, and more depleted isotopic signature than the gabbroic rocks ($^{87}\text{Sr}/^{86}\text{Sr}_i = 0.7054$ –0.7057, $\epsilon_{\text{Nd}}(t) = -4.67$ to -9.36). These features point to a source in a hydrous and less enriched SCLM.

The successive spatial–temporal association of mafic and felsic magma suites in the Guyang batholith attests to episodic crust–mantle interactions that occurred at depth, during ascent and emplacement and after emplacement, in the construction of high-K calc-alkaline plutons during the metacratonic evolution of the northern NCC, possibly in response to linear lithospheric delamination and hot asthenospheric upwelling along crustal-scale shear zones within a post-collisional transtensional regime of a passive continental margin.

© 2011 Elsevier B.V. All rights reserved.

1. Introduction

As the principal site of continental crustal growth and reworking, convergent plate margins constitute archives of most varied and extensive igneous activities occurred in all phases of an orogenic cycle in the model of plate tectonics. Thus their evolved tectonic regimes can

* Corresponding author at: State Key Laboratory of Lithospheric Evolution, Institute of Geology and Geophysics, Chinese Academy of Sciences, P.O. Box 9825, Beijing 100029, China. Tel.: +86 10 82998540.

E-mail address: zhangxh@mail.iggcas.ac.cn (X. Zhang).

be marked by the changes in the scale and compositions of the associated magmatic expressions (e.g., Barbarin, 1999; Bonin, 2004; Wang et al., 2004; Whalen et al., 2006). However, this differentiation is not always straight-forward, especially when a metacraton is introduced to refer to a craton that has been remobilized during an orogenic event (e.g., Abdelsalam et al., 2002; Ennih and Liégeois, 2008; Liégeois et al., 2003) and a distinct post-collisional geodynamic setting is integrated in plate tectonics model (e.g., Bonin, 2004; Liégeois, 1998). Complications mainly arise from ubiquitous occurrence of some tectonic setting-sensitive magmatic associations in all these regimes. For instance, medium to high-K calc-alkaline igneous rocks not only form essential components of continental arc magmatism, like the Mesozoic Sierra Nevada batholith in North America (e.g., Barbarin, 1991, 2005), but also constitute common magmatic expression during a metacratonic evolution of passive margins (Abdelsalam et al., 2002; De Waele et al., 2006; Fezaa et al., 2010; Liégeois et al., 2003). Moreover, numerous studies documented their presence in areas of extension post-dating active subduction (Altherr et al., 2000; Bonin, 2004; Clemens et al., 2009; Küster and Harms, 1998; Liégeois et al., 1998; Roberts et al., 2000; Topuz et al., 2010). For all such complexity, magmatism in a metacratonic passive margin is distinguishable from active continental arc one with its dominant cratonic geochemical signature (Abdelsalam et al., 2002; De Waele et al., 2006; Fezaa et al., 2010; Liégeois et al., 2003), while post-collisional magmatism is distinctive with more variable rock types due to intensified crust–mantle interactions, voluminous areal distribution as opposed to the commonly linearly distributed arc magmatism, free from collision-related metamorphism, and frequent linkage to horizontal movements along major shear zones (Bonin, 2004; Liégeois, 1998). Therefore, discriminating proper tectonic affiliation of questionable magmatism is essential for understanding the tectonic evolution of convergent plate margins.

In almost all potassic calc-alkaline granitoids worldwide (e.g. Altherr et al., 2000; Barbarin, 1991, 2005; Bonin, 2004; Poli and Tommasini, 1999; Slaby and Martin, 2008), ubiquitous mafic rocks commonly occur as different forms, such as independent mafic stock, rounded mafic microgranular enclave (MME) and undisturbed intrusive dyke. They generally attest to the essential role of mantle-derived melts in the initiation and evolution of calc-alkaline granitoid magma and signify the involvement of different stages of interactions between mafic and felsic magmas (Barbarin, 1991, 2005; Slaby and Martin, 2008; Vernon, 1984). Thus understanding their origin is of fundamental significance in elucidating the protracted physico-chemical interactions between magmas of different nature and/or origin during the construction of potassic calc-alkaline batholith.

The northern North China Craton (NCC) has been a convergent plate margin during the Paleozoic time, mainly in response to the rift–spread–extinction cycle of the Paleo-Asian Ocean to its north. This resulted in multiple episodes of Paleozoic magmatic events along the northern NCC (Zhang and Zhai, 2010, and references therein), with the Early Permian one being the most voluminous but also crucial for clarifying the Late Paleozoic orogenic cycle around the northern NCC. Depending on the ongoing controversial views about the timing of the final closure of the Paleo-Asian Ocean (Blight et al., 2010a; Chen et al., 2000; Jian et al., 2010; Xiao et al., 2003; Zhang et al., 2008, 2009a,b), different models have been proposed for its geodynamic setting. Some authors advocated an active continental arc setting (Zhang et al., 2009a,b), whereas others insisted on a post-collisional extensional regime (Luo et al., 2007, 2009; Zhang and Zhai, 2010; Zhang et al., 2008). Most recently, Jian et al. (2010) proposed a sequence of Permian tectonic–magmatic events in terms of the life cycle of a supra-subduction zone (SSZ)-type ophiolite based on the geochronological and geochemical study of the ophiolitic rocks from the Solonker suture zone.

Furthermore, uncertainties also revolve around the detailed mechanism through which this vast magmatic province has been constructed. This may partly be due to the lack of the multi-faceted approach in most current research strategies, and partly to the rare occurrence of whole

spectrum of mafic and felsic rocks that record the history of multiple stages of mafic and felsic magma interaction during its construction.

In this contribution, we present an integrated geochronological, petrologic and geochemical study performed on the Hercynian Guyang batholith from southern Inner Mongolia along the northern NCC in order to: 1) constrain the ages of various rock constituents of the batholith; 2) describe the systematic mineralogical and geochemical variations of various rock types; 3) trace their sources and characterize the petrogenesis of the main rock types; (4) document episodic mafic and felsic magma interaction during the construction of high-K calc-alkaline batholith and envision inherent geodynamic processes, as a contribution to our understanding of the controversial Late Paleozoic orogenic cycle around the northern NCC.

2. Geological background

The NCC is bounded on the north by the Central Asian Orogenic Belt (CAOB) (Sengör et al., 1993) and on the south by the Paleozoic to Triassic Qinling–Dabie–Sulu orogenic belt (Meng and Zhang, 2000) (Fig. 1a). It consists of two Archean continental blocks (Eastern and Western), separated by the Proterozoic Trans-North China orogenic belt (Zhao et al., 2001). The Eastern and Western blocks developed independently from the Late Archean to Early Paleoproterozoic and collided to form a coherent craton at ~1.85 Ga (Zhao et al., 2001). The NCC features a basement of dominantly Archean to Paleoproterozoic TTG (tonalitic–trondhjemitic–granodioritic) gneisses and metavolcanic and metasedimentary rocks, covered by Late Paleoproterozoic clastic sedimentary succession of Changcheng System and later intruded by occasional Mesoproterozoic mafic and carbonatitic dykes (Yang et al., 2011). Phanerozoic covers include Cambrian to middle Ordovician marine sedimentary rocks, Carboniferous–Permian continental clastic rocks and Mesozoic basin deposits (Kusky et al., 2007; Zhao et al., 2001).

To the north of the NCC, the generally EW-trending CAOB represents the giant accretionary orogen that extends from the Urals to the Pacific and from the Siberian and East European cratons to the North China and Tarim cratons (Fig. 1a) (Sengör et al., 1993; Windley et al., 2007). It mainly consists of island arcs, ophiolites, oceanic islands, accretionary wedges, oceanic plateaux and microcontinents comparable to that of Mesozoic–Cenozoic circum-Pacific accretionary orogens (Windley et al., 2007; Xiao et al., 2003).

The northern China–Mongolia tract covers a vast area from southern Mongolia to northern China, and lies along the middle-eastern segment of the CAOB. Its most prominent tectonic feature is the Solonker suture zone, which marks the final closure of the Paleo-Asian Ocean and separates two opposite-facing continental blocks (Fig. 1b) (Jian et al., 2010). The northern block includes the Hutag Uul Block of South Mongolia (Badarch et al., 2002) and the northern orogen (Early to Mid-Paleozoic) in northern China (Jian et al., 2008). The southern block comprises the southern orogen (Early to Mid-Paleozoic) and the northern margin of the NCC (Jian et al., 2010).

To the north of the Solonker suture, the basement geology of southern Mongolia is characterized by island-arc, arc basin and accretionary prism terranes that accreted around a postulated Precambrian cratonic block, i.e. the Hutag Uul Block (Badarch et al., 2002). These terranes record the tectonic evolution of the northern margin of the Paleo-Asian Ocean during the Paleozoic, generally interpreted to have taken place above a northward-dipping subduction zone (Windley et al., 2007). This leads to multiple phases of arc magmatic activities from Silurian to Late Carboniferous (Blight et al., 2010a,b; Lamb and Badarch, 2001; Yarmolyuk et al., 2008). They are subsequently intruded by voluminous latest Carboniferous to Early Permian peralkaline granites (Blight et al., 2010a; Kovalenko et al., 2006; Yarmolyuk et al., 2008). The Early to Mid-Paleozoic northern orogen of northern China is characterized by a metamorphic complex (Chen et al., 2009a), a SSZ-type ophiolitic sequence (Jian et al., 2008; Zhang et al., 2009c) and an overlying Late Devonian conglomerate. They are then intruded by

Carboniferous variably foliated calc-alkaline plutons (Bao et al., 2007; Chen et al., 2000; Liu et al., 2009), undeformed Early Permian A-type granites (Shi et al., 2004; Wu et al., 2002) and bimodal volcanic rocks (Zhang et al., 2008, 2011).

To the south of the Solonker suture, the Early to Mid-Paleozoic southern orogen includes the Ondor Sum subduction–accretion complex with blueschist, a SSZ-type ophiolite (ca. 497–477 Ma) and the Bainaimiao arc chain (ca. 488–438 Ma) (de Jong et al., 2006; Jian et al., 2008). It is separated from the NCC by the Chifeng–Bayan Obo fault.

During late Paleozoic time, the northern NCC experienced several magmatic events (Fig. 1c; Zhang and Zhai, 2010, and references therein), such as Middle Devonian mafic and alkaline intrusions (Zhang et al., 2009d, 2010a), Carboniferous foliated calc-alkaline plutons (Zhang et al., 2007, 2009a), Early Permian high-K calc-alkaline I-, S- and A-type granitoids (Zhang and Zhai, 2010, and references therein), and the latest Permian to Early Triassic high-K calc-alkaline to alkaline intrusive rocks (Zhang et al., 2009a, 2010b).

The Guyang region of southern Inner Mongolia is situated along the western segment of the northern NCC. This study area features a Precambrian basement and Phanerozoic tectono-magmatic events typical of the northern NCC. The basement comprises the lower amphibolite to granulite facies Archean gray tonalitic gneisses and greenstones of the Jining and Wulashan groups and the Late Paleoproterozoic low-grade metamorphic to unmetamorphosed rock sequences of the Zhaertai and Bayan Obo groups. The latter have a deposition time of ca. 1750 Ma and are commonly interpreted to be related to late Paleoproterozoic rift after cratonization of the NCC at ~1.85 Ga (Li et al., 2007). Paleozoic marine volcano-sedimentary sequences are sporadically distributed in the northern part of the area and extend into the neighboring CAOB. Mesozoic volcanic and continental sedimentary rocks, mainly of Jurassic and Early Cretaceous, occur primarily in basins developed unconformably on the Archean and Paleoproterozoic basement rocks.

Among numerous WE-, NE- and NW-trending fault systems present in the study area, four most prominent ones are Baotou–Huhhot, Guyang–Wuchuan, Chuanjing–Bulutai and Dahuabei–Damiao faults (Fig. 1b; Nie et al., 2002). The southernmost Baotou–Huhhot, fault zone constitutes a part of the WE-trending Daqingshan–Wulashan deep-seated fault belt (Davis et al., 1998) and is thought to be formed by a nappe movement during the Late Archean to Paleoproterozoic time (Li et al., 2007). Its reactivation during the Hercynian (350–300 Ma) tectonic events resulted in northvergent thrusting of the Archean to Paleoproterozoic metamorphosed volcanosedimentary sequences onto the Early Paleozoic volcano-sedimentary strata (Nie et al., 2002). The central Guyang–Wuchuan shear zone separates the Proterozoic meta-sedimentary rocks to the north from the Archean metamorphic rocks to the south. The northernmost Chuanjing–Bulutai fault constitutes a part of the Chifeng–Bayan Obo fault and defines the northern boundary of the NCC in this area. The Dahuabei–Damiao fault, the most prominent NE-trending one, extends more than 300 km and formed during the Late Paleozoic to Early Mesozoic time (Nie et al., 2002; Zhang et al., 1999).

Multiple phases of Phanerozoic igneous rocks intrude Archean and Paleoproterozoic metamorphic rocks at Guyang. However, they are not well constrained up to now due to few precise geochronological data. Based on the intrusive relationships, mineralogical and geochemical arguments, they appear to occur in four episodes: the Caledonian, Hercynian, Indonesian (Triassic) and Yanshannian (Jurassic and Cretaceous). The Caledonian granitoid suite is strongly deformed and partly migmatized with nearly EW-trending foliation. The Hercynian suite is represented by the Guyang batholith and consists of a few largely undeformed plutons. It is clearly intrusive into the Archean–Paleoproterozoic metamorphic rocks and the Caledonian granites, and is covered by the Early Cretaceous volcano-sedimentary strata of Guyang Formation (Fig. 1d). It is then intruded by Triassic granitic stocks and a number of Jurassic and Cretaceous mafic to felsic intrusive dykes.

3. Analytical methods

3.1. Mineral analysis

Major element compositions of minerals were measured on a JEOL JXA-8100 electron microprobe at the Institute of Geology and Geophysics, Chinese Academy of Sciences (IGGCAS). The operating conditions are: 15 kv accelerating voltage, 10 nA beam current and 3 μm spot diameter. Well-defined natural mineral standards are applied for calibration.

3.2. Zircon U–Pb dating

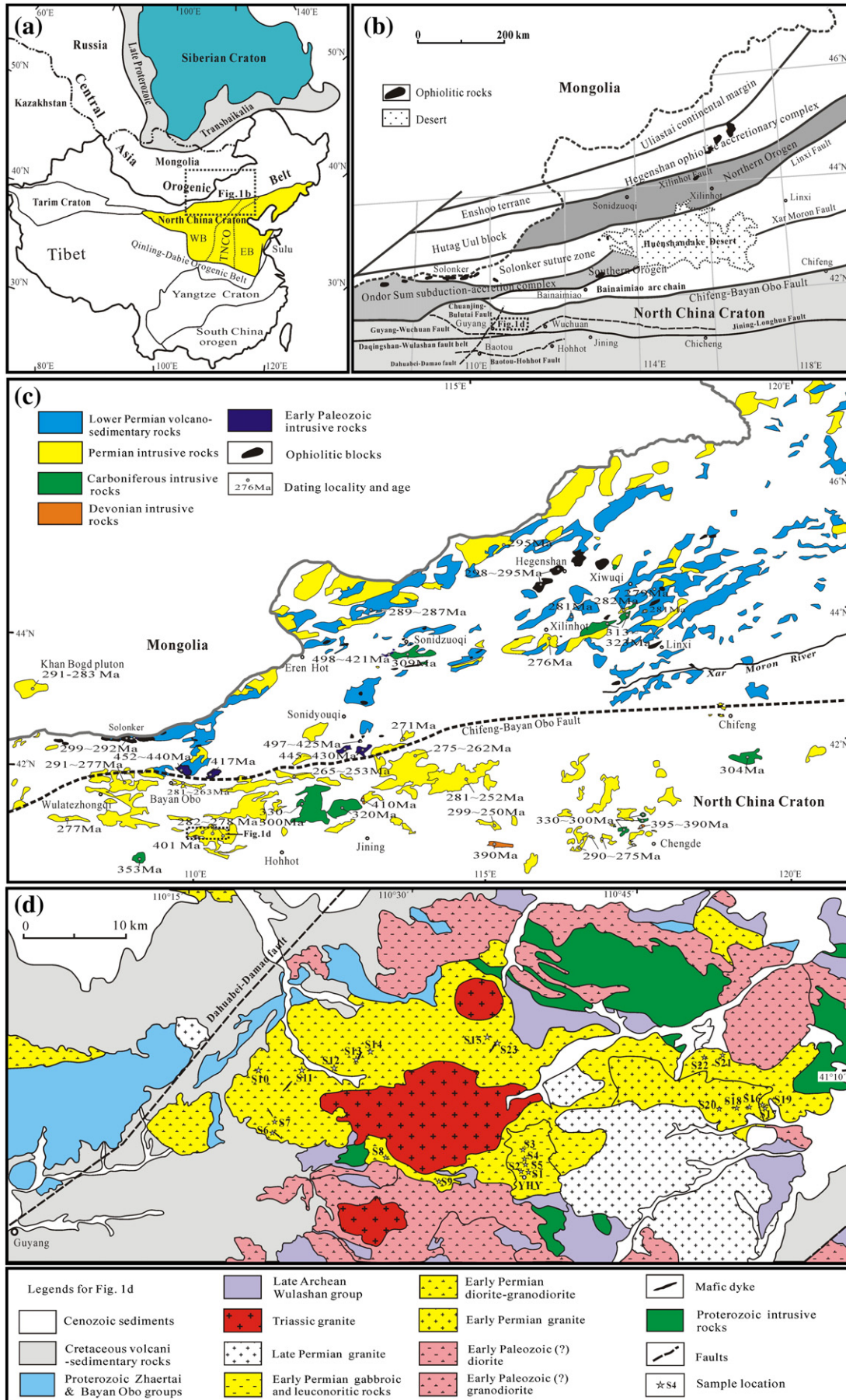
Zircons were separated from representative rock samples using standard density and magnetic separation techniques and purified by handpicking under a binocular microscope. Cathodoluminescence (CL) images were obtained for zircons prior to analyses, using a JXA-8100 microprobe at IGGCAS to reveal their internal structures.

Zircons from the gabbro, gabbroic diorite, diorite, granodiorite and MME were dated on an Agilent 7500a ICP-MS equipped with 193 nm laser, housed at the State Key Laboratory of Geological Processes and Mineral Resources, China University of Geosciences in Wuhan, China. Harvard zircon 91500 was used as a standard and the standard silicate glass NIST was used to optimize the machine. The spot diameter was 30 μm . The detailed analytical technique is similar to that described in Liu et al. (2010). The common-Pb corrections were made using the method of Anderson (2002) and the data were processed using the GLITTER (Griffin et al., 2008) and ISOPLOT (Ludwig, 2001) programs.

Zircon U/Pb dating for monzogranite sample was conducted using the Chinese Academy of Sciences Cameca IMS-1280 ion microprobe (CASIMS) at the Institute of Geology and Geophysics in Beijing, following analytical procedures described in Li et al. (2009). A primary ion beam of ca. 8 nA, 13 kV O_2^- and ca. 20–30 μm spot diameter was used during the analysis. Pb/U calibration was performed relative to the 1065 Ma standard zircon 91500 with Th and U concentrations of ca. 29 and 81 ppm respectively (Wiedenbeck et al., 1995). Correction of common lead was made by measuring ^{204}Pb . An average Pb of present-day crustal composition (Stacey and Kramers, 1975) is used for the common Pb assuming that it is largely due to surface contamination introduced during sample preparation. Individual analyses by both LA-ICPMS and SIMS are reported with 1σ uncertainties.

3.3. Hornblende Ar/Ar dating

After heavy liquid separation the hornblende from the mafic dyke was washed with acetone in an ultra-sonic bath for 20 min and rinsed several times with acetone. Cleaned hornblende was wrapped in Al foil and irradiated together with Ga1550-biotite standards, optical CaF_2 and K-glass monitors in position H8 of the 49–2 reactor, Beijing, China, for 47.5 h with 0.5 mm cadmium foil shield. $^{40}\text{Ar}/^{39}\text{Ar}$ step-heating analysis by furnace was performed at the IGGCAS, on a MM5400 mass spectrometer operating in a static mode. The total system blanks were in the range of $4.9\text{--}5.8 \times 10^{-16}$ mol for mass 40, $0.9\text{--}1.4 \times 10^{-18}$ mol for mass 39, $8.7\text{--}9.2 \times 10^{-19}$ mol for mass 37, and $1.8\text{--}2.1 \times 10^{-18}$ mol for mass 36. Ca, K correction factors were calculated from the CaF_2 and K-glass monitors: $(^{40}\text{Ar}/^{39}\text{Ar})_{\text{K}} = 1.13 \times 10^{-2}$, $(^{39}\text{Ar}/^{37}\text{Ar})_{\text{Ca}} = 7.24 \times 10^{-4}$, $(^{36}\text{Ar}/^{37}\text{Ar})_{\text{Ca}} = 2.39 \times 10^{-4}$. The data were corrected for system blanks, mass discriminations, interfering Ca, K derived argon isotopes, and the decay of ^{37}Ar since the time of the irradiation. The decay constant used throughout the calculations is $\lambda = (5.543 \pm 0.010) \times 10^{-10} \times \alpha^{-1}$, as recommended by Steiger and Jäger (1977). Details of the step-heating analysis were outlined by He et al. (2004). The plateau and isochron ages were calculated using ArArCALC (Koppers, 2002). Error assignments of isotope ratios and ages are $\pm 1\sigma$.



3.4. Major and trace element analysis

For geochemical and isotopic analyses, samples were ground in an agate mill to ~200 mesh. Major oxides were analyzed with a Phillips PW 2400 X-Ray fluorescence spectrometer (XRF) at the IGGCAS. Trace element abundances were obtained on a VG-PQII ICP-MS also at the IGGCAS. Samples were dissolved in distilled HF + HNO₃ in 15 ml high-pressure Teflon bombs at 120 °C for 6 days, dried and then diluted to 50 ml for analysis. A blank solution was prepared and the total procedural blank was <50 ng for all trace elements. Indium was used as an internal standard to correct for matrix effects and instrument drift. Precision for all trace elements is estimated to be 5% and accuracy is better than 5% for most elements by analyses of the GSR-3 standard.

3.5. Whole-rock Sr–Nd isotopic analysis

Sr and Nd isotopic compositions were measured on a Finnigan Mat 262 thermal ionization mass spectrometer at the IGGCAS, following the procedure described in Zhang et al. (2008). Procedural blanks were <100 pg for Sm and Nd and <500 pg for Rb and Sr. ¹⁴³Nd/¹⁴⁴Nd was corrected for mass fractionation by normalization to ¹⁴⁶Nd/¹⁴⁴Nd = 0.7219, and ⁸⁷Sr/⁸⁶Sr ratios were normalized to ⁸⁶Sr/⁸⁸Sr = 0.1194. The measured values for the BCR-2 Nd standard and BCR-2 Sr standard were ¹⁴³Nd/¹⁴⁴Nd = 0.512641 ± 0.000010 (2σ, n = 4) and ⁸⁷Sr/⁸⁶Sr = 0.705018 ± 0.000011 (2σ, n = 4) during the period of data acquisition.

3.6. In situ Hf isotopic analysis

In situ zircon Hf isotopic analyses were conducted using the Neptune MC-ICP-MS, equipped with a 193-nm laser at the IGGCAS. Spot size of 32 μm was used for analysis, with a laser repetition rate of 10 Hz at 100 mJ. The detailed analytical procedure and correction for interferences follow those described by Wu et al. (2006). During analyses, the ¹⁷⁶Hf/¹⁷⁷Hf and ¹⁷⁶Lu/¹⁷⁷Hf ratios of the standard zircon (91500) were 0.282270 ± 0.000023 (2σ, n = 15) and 0.00028, similar to the commonly accepted ¹⁷⁶Hf/¹⁷⁷Hf ratio of 0.282284 ± 0.000003 (1σ) measured using the solution method (Woodhead et al., 2004).

4. Petrography and mineral chemistry

With a roughly east–west trending and an outcrop coverage of over 700 km² (Fig. 1d), the Hercynian Guyang batholith consists of dominant dioritic to granodioritic plutons of varying size with abundant MME and synplutonic mafic dykes, and subordinate gabbroic and monzogranitic stocks. Representative analyses of the main mineral phases for various lithologies are reported in the Online Supplemental Table 1.

The gabbroic stock is located at Yuanhengyong (YHY) along the southern margin of the batholith and intrudes the Neo-Archean gneisses (Yuan and Wang, 2006). It mainly consists of gabbro, gabbroic diorite and leuconorite. Gabbros and gabbroic diorites are massive, fine- to medium-grained with subophitic textures. They typically contain 15–25% orthopyroxene and clinopyroxene, 50–65% plagioclase, subordinate hornblende and biotite, with accessory amounts of interstitial K-feldspar, quartz, magnetite, zircon, apatite and titanite. Phenocrystic clinopyroxene is dominantly augite and occasionally diopside, with a reconstructed composition Wo_{26–46}En_{32–51}Fs_{21–32}. Orthopyroxene

commonly occurs as granular and lamellar exsolution within clinopyroxene, and has a composition Wo_{1–6}En_{43–50}Fs_{47–53}. Plagioclase crystals are slightly zoned with a compositional range from An_{40–56}Ab_{42–59}Or_{1–2} (core) to An_{38–52}Ab_{41–58}Or_{1–3} (rim). They commonly form an interlocking framework with interstitial perthitic orthoclase (Or_{88–94}Ab_{7–11}An_{0–2}). Leuconorites are fine- to medium-grained with a cumulate texture, and are composed of 60–80% plagioclase (An_{81–86}Ab_{14–19}), 10–25% hornblende (tschermakite, X_{Mg}[Mg/(Fe + Mg)] = 0.77–0.91), 5–10% clinopyroxene (mainly diopside), 1–5% biotite (X_{Mg} = 0.4–0.48), and minor magnetite, apatite, zircon, titanite and ilmenite.

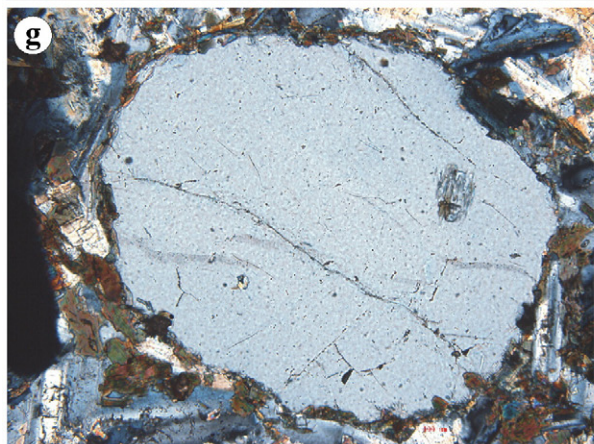
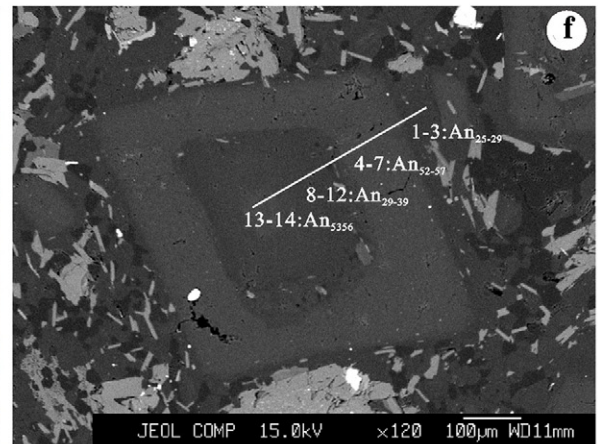
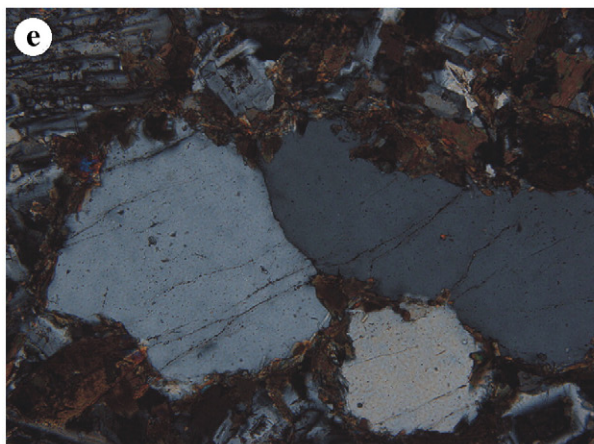
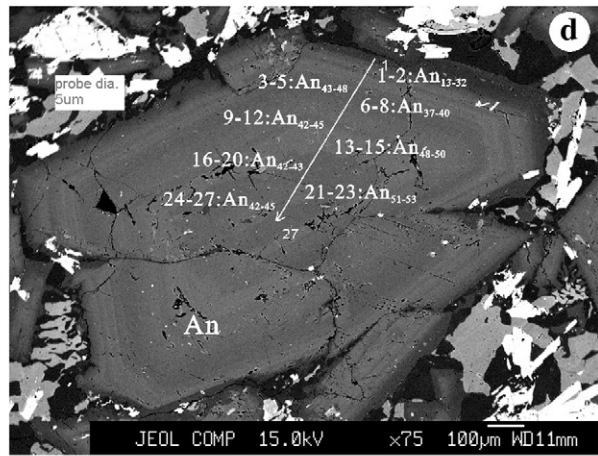
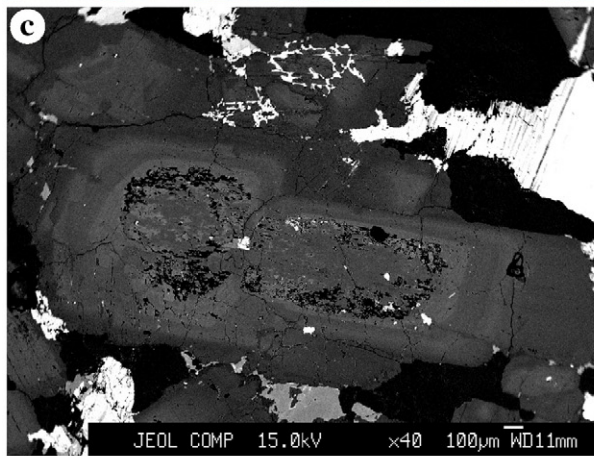
Diorites and quartz diorites are fine to medium-grained with hypidiomorphic equigranular textures. They contain abundant MME, clots of mafic minerals and mafic dykes (Fig. 2a and b). Their major mineral constituents include 45–60% plagioclase, 20–25% hornblende, 5–10% biotite, 5–8% K-feldspar and 3–15% quartz. Accessory phases are pyroxene, titanite, magnetite, apatite and zircon. Hornblende mainly occurs as subhedral to euhedral phenocrysts. It shows a narrow range of X_{Mg} = 0.52–0.64 and mainly belongs to magnesio-hornblende in the classification scheme of Leake et al. (1997). Plagioclase is subhedral to euhedral with variable zones. Some grains display normal oscillatory zoning with a composition range from An_{31–46}Ab_{52–70}Or_{0–2} (core) to An_{21–41}Ab_{55–79}Or_{1–2} (rim), while some show a complex zoning pattern with resorption–regrowth textures (Fig. 2c). K-feldspar occurs as subhedral to anhedral interstitial phase, with a composition of Or_{90–95}Ab_{4–11}An_{0–1}. Biotite is present as subhedral, strongly pleochroic flakes, with a composition characterized by moderate Al contents and variable X_{Mg} of 0.43–0.55.

With the amount of K-feldspar increasing, diorites can grade into medium to coarse-grained hypidiomorphic granodiorites. Typical samples comprise 40–55% plagioclase, 5–15% K-feldspar, 15–25% quartz, 5–15% biotite, 3–10% hornblende, and accessory epidote, zircon, titanite, magnetite and apatite. The textures and compositions of major constituents are similar to those of the diorites: variably zoned plagioclase (Fig. 2d, Online Supplemental Table 2), subhedral to anhedral perthitic orthoclase (Or_{90–97}Ab_{3–7}), green magnesio-hornblende with X_{Mg} of 0.50 to 0.62, subhedral flaky biotite with X_{Mg} of 0.52 to 0.55.

The granite facies crops out in the eastern part of the batholith and is a fine- to medium-grained, equigranular biotite monzogranite. Typical samples comprise 25–35% K-feldspar, 30–35% plagioclase, 30–40% quartz, 4–12% biotite, and accessory zircon, apatite, magnetite and allanite. K-feldspar mainly occurs as perthitic orthoclase (Or_{89–96}Ab_{4–11}) with large subhedral to anhedral grains. Plagioclase (An_{5–35}Ab_{64–95}Or_{0–2}) is chiefly present as coarse albite exsolution within alkali feldspar. Quartz mainly forms aggregates of large phenocrysts. Subhedral to anhedral biotite (X_{Mg} = 0.36–0.5) is interstitial to K-feldspar and quartz.

MME are commonly centimeter to meter-sized with lobate or ellipsoidal shapes (Fig. 2a), suggesting a molten state during enclosure in colder host magma. They have a gabbroic to monzodioritic composition, and mainly consist of a fine- to medium-grained assemblage of 10–20% euhedral–subhedral green hornblende (magnesio-hornblende, X_{Mg} = 0.61–0.65), 25–35% subhedral plagioclase, 10–25% biotite (X_{Mg} = 0.50–0.54), 5–10% anhedral K-feldspar, minor quartz and clinopyroxene, and accessory titanite, ilmenite, magnetite, apatite and zircon. Plagioclase megacrysts are complexly zoned. Globular quartz grains commonly exhibit a typical ocellar textures with spheric shape

Fig. 1. (a) Tectonic framework of the North China–Mongolian segment of the Central Asian Orogenic Belt (modified after Jahn, 2004) and major tectonic divisions of China, where YZ and SC denote the Yangtze Craton and South China orogen. Also shown are the subdivisions of the North China Craton (Zhao et al., 2001), where EB, TNCO and WB denote the Eastern block, Trans-North China orogen and Western block, respectively. (b) Sketch tectonic map of the northern North China–Mongolia tract (modified after Badarch et al., 2002; Jian et al., 2008; Xiao et al., 2003). (c) Sketch geological map of the northern North China showing distribution of the Paleozoic magmatic rocks (modified after Zhang and Zhai, 2010). (d) Geological sketch map of the Guyang area (modified from INMGMR, 1972), with the sample locations shown. The samples collected at each locality are as follows: S1: NM56, NM57, NM58, NM59, and NM62; S2: NM67, NM68, NM58, NM59, and NM62; S3: NM73, NM74, and NM76; S4: NM77 and NM79; S5: NM84; S6: NM86, NM87, NM88, NM94, and NM96; S7: NM97 and NM100; S8: NM104, NM106, and NM108; S9: NM138; S10: NM142 and NM143; S11: NM144; S12: NM145/1, NM145/2, and NM145/3; S13: NM146 and NM147; S14: NM151 and NM152; S15: NM153; S16: NM156; S17: NM159; S18: NM161 and NM162; S19: NM167; S20: NM168; S21: NM173; S22: NM181 and NM183; and S23: NM08-1. YHY = Yuanhengyong.



and hornblende mantle (Fig. 2e). Clots of mafic and accessory minerals are also a common feature of the MME. They consist mainly of euhedral hornblende crystals intergrown with biotite and opaque minerals.

Mafic dykes are tens of centimeters to several meters in width and tens to several hundred meters in length (Fig. 2b). They commonly have a gabbroic dioritic to dioritic composition, and show an ophitic or porphyritic texture with phenocrysts of plagioclase and hornblende (2–3.5 mm) in a fine-grained matrix of 40–50% plagioclase, 25–35% hornblende, 10–15% biotite, 5% K-feldspar, and minor quartz, clinopyroxene, magnetite, ilmenite, zircon and apatite. Plagioclase phenocrysts are characterized by both simple concordant zones and complex zoning pattern (Fig. 2f). Quartz ocelli are also common (Fig. 2g). Hornblende is tschermakite with X_{Mg} of 0.73 to 0.88. Locally, mafic dykes contain angular xenoliths of the host granodiorite (Fig. 2h).

5. Geochronological and geochemical data

5.1. Zircon U–Pb data

The results of zircon U–Pb analyses are listed in the Online Supplemental Table 3. Sample NM07-56 is a gabbroic diorite collected from the YHY stock. Zircons from this sample are mostly clear, subhedral stubby prisms. They are about 80 to 210 μm in length, with length-to-width ratios of 1.2 to 2 (Fig. 3a). Twenty-one analyses were conducted on 21 zircon grains. Measured U concentrations vary from 220 to 1515 ppm, and Th from 183 to 1305 ppm. All analyses have Th/U ratios of 0.64–1.14. Among them, five spots define a concordia age of 286.4 ± 2.8 Ma (MSWD of concordance = 1.2), while the other ten concordant zircons yield an age of 277.2 ± 1.9 Ma with a much lower MSWD (0.28) (Fig. 4a).

Sample NM07-73 is a gabbro also collected from the YHY stock. Zircons from this sample are colorless or light brown with no inclusions. They are mostly sub-euhedral prismatic crystals with 70–180 μm in size. In CL images, they commonly show internal oscillatory zoning (Fig. 3b). Twenty analyses on 20 zircon grains result in U concentrations from 43.5 to 153 ppm, Th from 15.4 to 166 ppm and Th/U ratios of 0.29–1.01. Among them, eleven spots define a concordia age of 279.5 ± 1.9 Ma with an MSWD of 1.6 (Fig. 4b).

Sample NM07-144 is a granodiorite from the main body of the batholith. Zircons from this sample are mostly clear, euhedral to subhedral, stubby to elongate prisms. They are about 60 to 240 μm long with length-to-width ratios between 1.5:1 and 3:1. The euhedral zircons mostly show clear magmatic oscillatory zoning (Fig. 3c). All analyses yield U concentrations from 93 to 330 ppm, Th from 69 to 404 ppm and Th/U ratios from 0.55 to 1.22. Ten spots define a concordia age of 280.3 ± 1.9 Ma with an MSWD of 0.62 (Fig. 4c).

Sample NM07-145 is a MME collected from the dioritic unit of the batholith. Zircons from this sample are clear, euhedral to subhedral, stubby to elongate prisms. They are about 60 to 180 μm long with well-developed oscillatory zoning (Fig. 3d). Measured U concentrations from 21 grains vary from 108 to 253 ppm, and Th ranges from 77 to 233 ppm. All analyses have Th/U ratios of 0.61–1.09 and fifteen concordant zircons yield an age of 280.7 ± 1.6 Ma with an MSWD of 7 (Fig. 4d).

Sample NM07-181 is a diorite collected from the eastern part of the batholith. Zircons from this sample are euhedral to subhedral prisms with clear oscillatory zoning (Fig. 3e). Twenty-five analyses from this sample were conducted on 25 grains during a single analytical session. Measured U concentrations vary from 69 to 335 ppm, and Th from 57 to 191 ppm. All analyses have Th/U ratios of 0.37–0.67 and twenty one spots define a concordia age of 279 ± 1.4 Ma with an MSWD of 0.45 (Fig. 4e).

Zircons from monzogranite sample NM07-156 are colorless or light brown with no inclusions. They are 70–180 μm in size and mostly euhedral to subhedral prismatic crystals. In CL images, they show common internal oscillatory zoning (Fig. 3f). Fifteen measured grains from this sample yield U concentrations from 142 to 1040 ppm, and Th from 77 to 474 ppm. With the exception of the point 5, the other analyses have Th/U ratios of 0.49–1.50. Fifteen spots define a concordia age of 281.5 ± 2.1 Ma with an MSWD of 0.15 (Fig. 4f).

5.2. Hornblende $^{40}\text{Ar}/^{39}\text{Ar}$ data

$^{40}\text{Ar}/^{39}\text{Ar}$ analytical data for hornblende separates from the mafic dyke sample NM07-94 are listed in Table 1. As shown in Fig. 5a, the hornblende sample yields a nearly concordant age spectrum. Five consecutive steps, which account for 83.6% of the total ^{39}Ar released, define a plateau age of 275.9 ± 2.1 Ma, with an MSWD of 4.28. An inverse isochron age of 274.7 ± 3.3 Ma, calculated from all steps that formed the plateau (Fig. 5b), is in agreement with the plateau age. The $^{40}\text{Ar}/^{36}\text{Ar}$ intercept of 318.0 ± 26.6 is not distinguishable from the air ratio.

5.3. Major oxides and trace elements

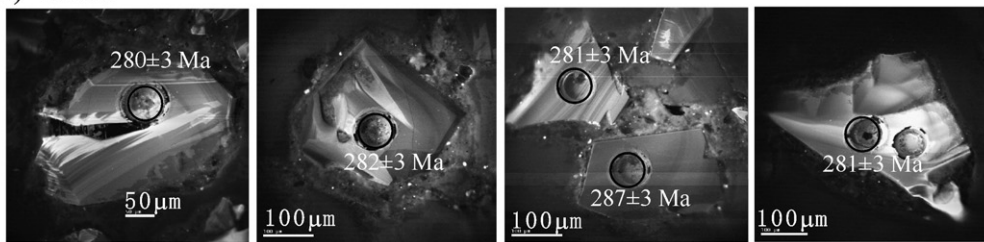
Whole-rock major and trace element compositions for various lithologies of the Guyang batholith are presented in Online Supplemental Table 4. As shown on the $\text{K}_2\text{O} + \text{Na}_2\text{O}$ vs. SiO_2 diagram (Le Maitre, 2002) (Fig. 6a), the samples from these lithologies display a roughly continuous geochemical distribution from gabbro to granite. They exhibit a medium to high-K calc-alkaline character on the SiO_2 vs. K_2O plot (Fig. 6b). On the alkali–lime index (MALI = $\text{NaO} + \text{KO} - \text{CaO}$ by wt.) plot of Frost et al. (2001) (Fig. 6c), they mainly belong to calc-alkali series.

In most major-element Harker plots (Fig. 7), with the exception of the leuconorites, most samples from the batholith define a roughly correlated evolution trend: CaO , Al_2O_3 , MgO , TFe_2O_3 , TiO_2 , MnO , and P_2O_5 are negatively correlated with SiO_2 , while K_2O and Na_2O positively correlated. Likewise, compatible elements such as Sc, Co, Cr and V decrease with increasing SiO_2 (Fig. 8), a feature also shared by Sr and Y. Rb, Ba, Pb and U show a roughly positive correlation with SiO_2 (Fig. 8). Abundances of some high field strength element (HFSE) such as Zr, Hf, Nb, Ta and rare earth element like La and Nd display no clear trend with increasing SiO_2 (Fig. 8).

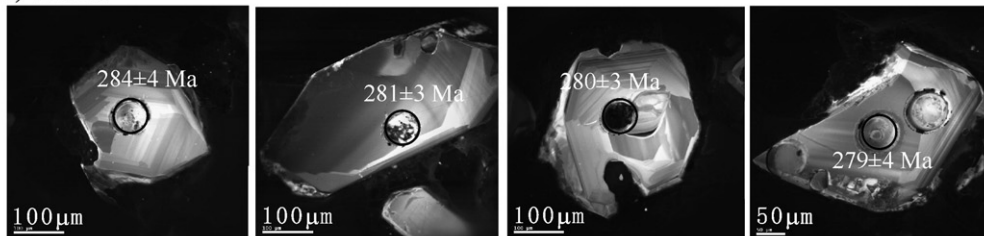
Specifically, the samples from the YHY gabbroic stock mainly plot in the fields of gabbro and gabbroic diorite. The gabbros and gabbroic diorites have SiO_2 contents ranging from 52.7 to 55.1%, with high abundances of total Fe_2O_3 (5.94–10.94%), Al_2O_3 (17.58–22.09%), K_2O (1.5–2.2%) and CaO (7.02–8.09%), low contents of TiO_2 (0.71–1.36%), P_2O_5 (0.30–0.53%), and various concentrations of MgO (1.99–4.15%). Their Mg-number ranges from 39 to 45. The rocks exhibit a transitional character between medium- and high-K calc-alkaline, with aluminum saturation index [ASI = molar $\text{Al}_2\text{O}_3/(\text{CaO} + \text{K}_2\text{O} + \text{Na}_2\text{O})$] of 0.81 to 0.99 (Fig. 6d). With respect to trace elements, they are characterized with moderate LREE enrichment ($\text{La}_N/\text{Yb}_N = 9.54$ to 15.4) and small negative or positive Eu anomalies ($\text{Eu}/\text{Eu}^* = 0.71$ –1.16; Fig. 9a). In the primitive mantle (PM)-normalized trace element diagrams (Fig. 9b), they are typified with enrichment in large ion lithophile elements (LILE, such as Sr, Ba, and Rb) relative to LREE and HFSE (such as Nb, Ta, P and Ti). By contrast, the leuconorites have SiO_2 of 43.2 to 44.4% and Mg-number from 68 to 71. They show high contents of Al_2O_3 and CaO , and moderate concentrations of Cr and Ni. They have low REE contents (with

Fig. 2. Representative field and thin-section photographs of various hybridization textures in the Guyang batholith. (a) Strongly flow-aligned mafic microgranular enclaves (MME) occurring within diorite and granodiorite. (b) Undisturbed mafic dykes within diorite. (c) Complexly zoned plagioclase with patchy interiors from quartz diorite NM106. (d) Complexly zoned plagioclase from granodiorite NM152 (Online Supplemental Table 2). (e) Quartz-hornblende ocelli in hybrid MME (NM145). (f) Complexly zoned plagioclase from mafic dyke NM94 (Online Supplemental Table 2). (g) Quartz-hornblende ocelli in mafic dyke (NM147). (h) Angular quartz diorite xenolith within mafic dyke. Hammer is 35 cm long and pen is 15 cm.

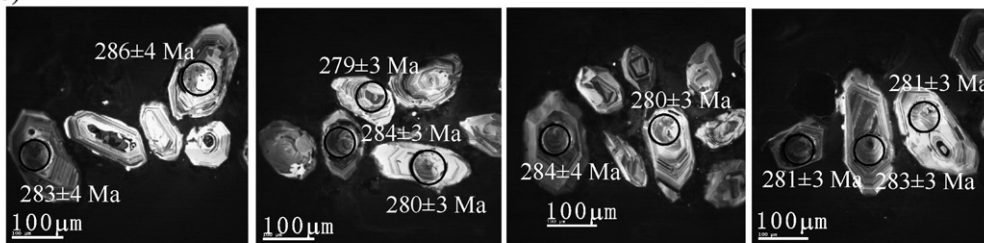
(a) NM56



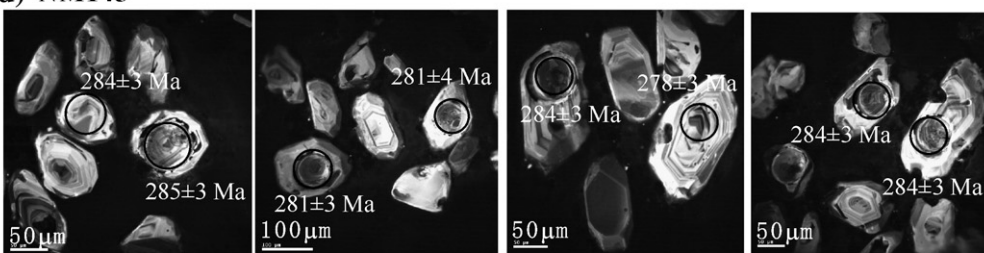
(b) NM73



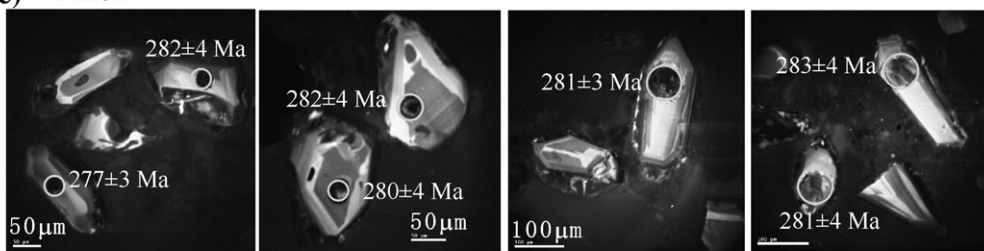
(c) NM144



(d) NM145



(e) NM181



(f) NM156

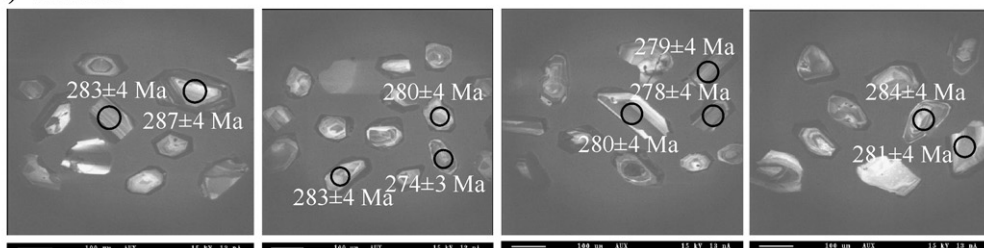


Fig. 3. Cathodoluminescence (CL) images of the dated zircons from various rock types in the Guyang batholith.

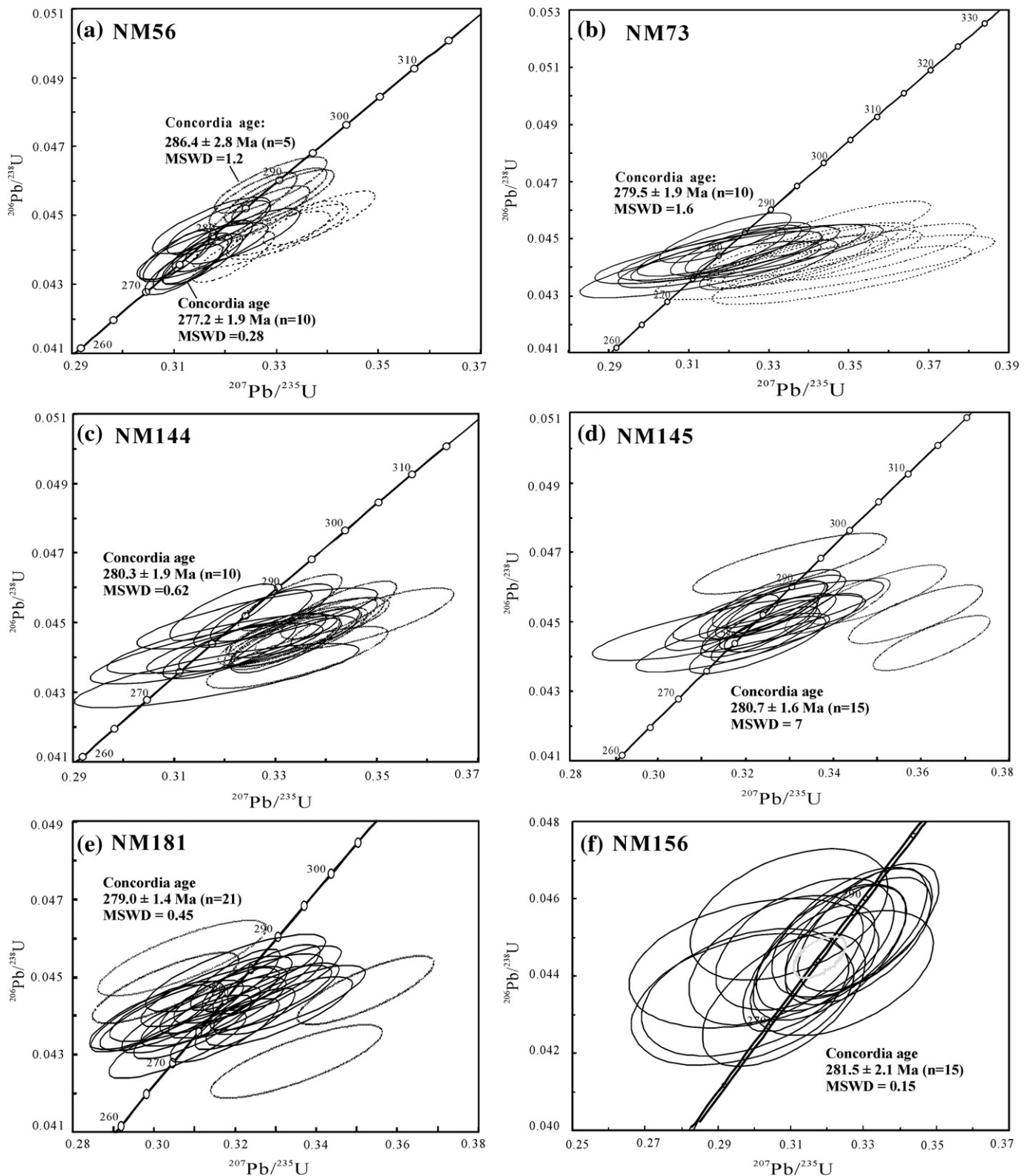


Fig. 4. U–Pb zircon concordia diagrams for various rock types in the Guyang batholith.

$La_N/Yb_N = 11.1$ to 13.1) and conspicuous positive Eu anomalies ($Eu/Eu^* = 2.68$ – 3.86) (Fig. 9a). They also exhibit distinctive PM-normalized trace element patterns from the gabbroic rocks (Fig. 9b), with conspicuous depletion in Th, U, Zr and Hf.

The samples from the main body of the batholith plot in the fields of diorite and granodiorite. They range in SiO_2 content from 56.4 to

68.2%, with Mg-number from 42 to 56. Most samples show a high-K calc-alkaline character and are metaluminous with A/CNK from 0.88 to 1.05 (Fig. 6d). The rocks display regular trends of increasing Al_2O_3 , K_2O , Na_2O , and P_2O_5 and decreasing CaO , MgO , TFe_2O_3 , TiO_2 , MnO , Sc , Co and V with increasing SiO_2 (Figs. 7 and 8). With regard to trace elements, they are characterized by low Cr and Ni, variable Rb and Zr,

Table 1
Argon isotopic results of hornblendes from the mafic dykes of the Guyang batholith.

T (°C)	⁴⁰ Ar/ ³⁹ Ar	³⁷ Ar/ ³⁹ Ar	³⁶ Ar/ ³⁹ Ar	⁴⁰ Ar*/ ³⁹ Ar _k	⁴⁰ Ar* (%)	³⁹ Ar _k (% of cum)	Age (Ma)	±2σ
800 °C	29.18822	0.45563	0.04507	15.912191	54.49	0.23	170.66	± 18.03
880 °C	146.28986	0.83538	0.40742	25.983672	17.75	1.21	270.91	± 29.26
930 °C	46.92568	0.34184	0.07244	25.554787	54.44	2.88	266.75	± 6.13
980 °C	48.76678	0.40106	0.07937	25.353733	51.97	5.04	264.80	± 6.57
1030 °C	49.86077	0.49900	0.08077	26.044318	52.21	7.89	271.50	± 6.69
1070 °C	28.52000	1.14146	0.00993	25.701184	90.03	13.86	268.17	± 2.19
1100 °C	27.24310	2.54434	0.00452	26.166944	95.84	25.60	272.69	± 1.96
1130 °C	27.09075	3.26696	0.00327	26.457978	97.39	45.33	275.50	± 1.62
1160 °C	26.87157	3.60907	0.00243	26.523442	98.40	75.36	276.13	± 1.70
1190 °C	29.75741	3.29313	0.01132	26.750038	89.64	81.08	278.32	± 2.25
1250 °C	28.06433	3.96394	0.00623	26.627924	94.56	97.41	277.14	± 1.74
1320 °C	30.85928	4.04985	0.01382	27.190869	87.81	99.25	282.56	± 3.09
1450 °C	30.18082	3.69528	0.01586	25.870510	85.45	100.00	269.82	± 10.33

but with high Sr and Ba abundances. In the chondrite-normalized REE diagrams (Fig. 9c), they show LREE-enriched patterns ($La_N/Yb_N = 5.68–37.2$), with minor negative or positive Eu anomalies ($Eu/Eu^* = 0.76–1.13$). In the PM-normalized trace element patterns (Fig. 9d), they show enrichment in LILE and LREE and strong depletion in HFSE.

In the MME, SiO₂ contents range between 49.2 and 54.7% and Mg-number between 50 and 61, while Al₂O₃ contents vary from 15.3 to 18.3%, CaO from 7.2 to 8.0% and Na₂O from 3.4 to 3.8%. The enclaves have relatively high concentrations of Cr (55–325 ppm) and V (156–208 ppm). They are metaluminous with A/CNK ranging from 0.70 to 0.82 (Fig. 6d). The REE patterns for the MME are relatively homoge-

neous, with high LREE ($174 > La_N > 111$), moderate HREE ($17 > Yb_N > 9$) and minor negative Eu anomalies ($Eu/Eu^* = 0.73–0.98$) (Fig. 9e). In the PM-normalized diagrams (Fig. 9f), the MME show positive anomalies in LILE and negative anomalies in HFSE.

The mafic dykes have SiO₂ contents ranging from 52.9 to 57.9%, with high abundances of total Fe₂O₃ (6.8–8.0%) and CaO (5.6–6.8%), low contents of TiO₂ (0.77–0.96%) and P₂O₅ (0.26–0.38%), and various concentrations of MgO (1.98–7.38%), Cr (3–338 ppm) and Ni (6–120 ppm). Their Mg-number ranges from 35 to 65. They are metaluminous with A/CNK from 0.82 to 0.97 (Fig. 6d). For trace elements, most samples exhibit similar REE and RE abundances to those of the MME (Fig. 9g and h), with moderately enriched LREE ($La_N/Yb_N = 9.5–20.7$), slight negative Eu anomalies, enriched LILE and depleted HFSE. However, two exceptional samples are distinctive with their steeply inclined REE patterns ($La_N/Yb_N = 96$ to 102) and extremely low heavy REE contents ($Yb_N < 1$).

The equigranular granites have a restricted SiO₂ range from 74.3 to 75.6%, with high Al₂O₃ (13.7–15.4%) and alkalis ($K_2O + Na_2O = 7.5–9.6\%$), and low MgO and TiO₂ concentrations. They are peraluminous with A/CNK of 1.03 to 1.1 (Fig. 6d). In the chondrite-normalized REE diagrams (Fig. 9i), they are enriched in LREE ($La_N/Yb_N = 14.5–50.1$), with minor Eu anomalies ($Eu/Eu^* = 0.89–1.36$; Online supplemental Table 4) and depleted in HREE and Y. In the PM-normalized trace element diagrams (Fig. 9j and b), they show enrichment in LILE and LREE and strong depletion in HFSE. High concentrations in Sr and La and low contents in Y and Yb result in high Sr/Y and La/Yb ratios, and so the samples exclusively fall within the adakite field on $(La/Yb)_N–Yb_N$ and Sr/Y–Y diagrams (not shown).

5.4. Whole rock Sr–Nd isotopes

Whole-rock Sr–Nd isotope analytical data, together with the calculated initial Sr–Nd isotopic compositions at age of 280 Ma, are presented in Table 2.

As shown in a plot of $\epsilon_{Nd}(t)$ vs. $^{87}Sr/^{86}Sr_i$ (Fig. 10), gabbroic diorite and leuconorite samples have a restricted range of isotopic compositions with $^{87}Sr/^{86}Sr_i$ ratios of 0.70461 to 0.70532, moderately negative $\epsilon_{Nd}(t)$ values of -7.73 to -10.2 and model ages (T_{DM}) of 1654 to 1851 Ma. Diorites and granodiorites exhibit initial $^{87}Sr/^{86}Sr$ ratios from 0.70499 to 0.70639, relatively wide $\epsilon_{Nd}(t)$ range from -8.36 to -13.9 and model ages (T_{DM}) of 1583 to 2381 Ma. Four MME samples are characterized with $^{87}Sr/^{86}Sr_i$ ratios from 0.70494 to 0.70566, moderately negative $\epsilon_{Nd}(t)$ values of -8.48 to -10.1 and model ages (T_{DM}) of 1689 to 1906 Ma. Mafic dyke samples have $^{87}Sr/^{86}Sr_i$ ratios from 0.70545 to 0.70569, $\epsilon_{Nd}(t)$ values of -4.67 to -9.36 and model ages (T_{DM}) of 1444 to 1804 Ma. Monzogranites have $^{87}Sr/^{86}Sr_i$ ratios from 0.7053 to 0.70553, negative $\epsilon_{Nd}(t)$ values of -10.5 to -11.3 and model ages (T_{DM}) of 1478 to 1741 Ma.

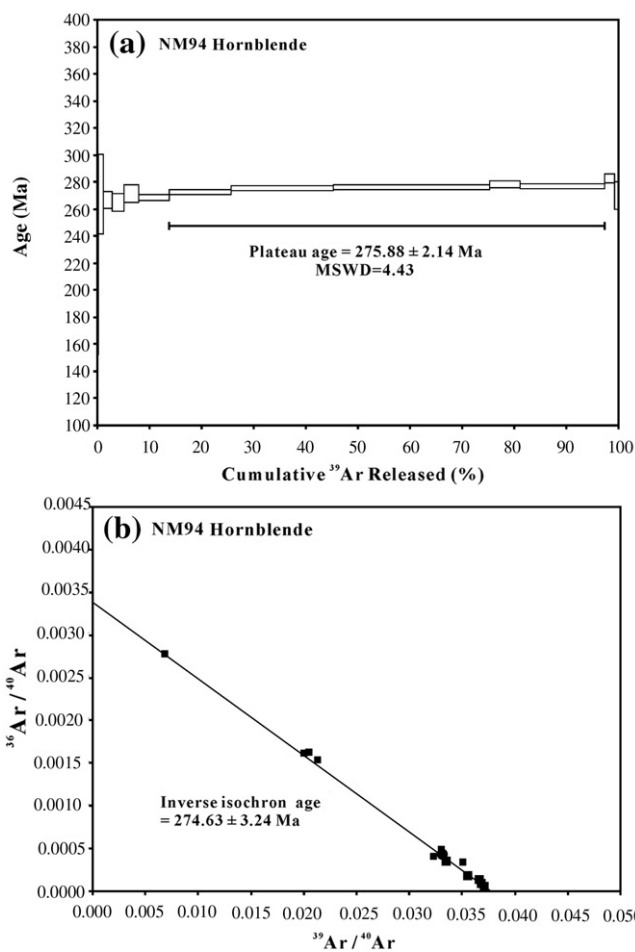


Fig. 5. ⁴⁰Ar/³⁹Ar age spectra and isochron plots for hornblende from the mafic dyke in the Guyang batholith.

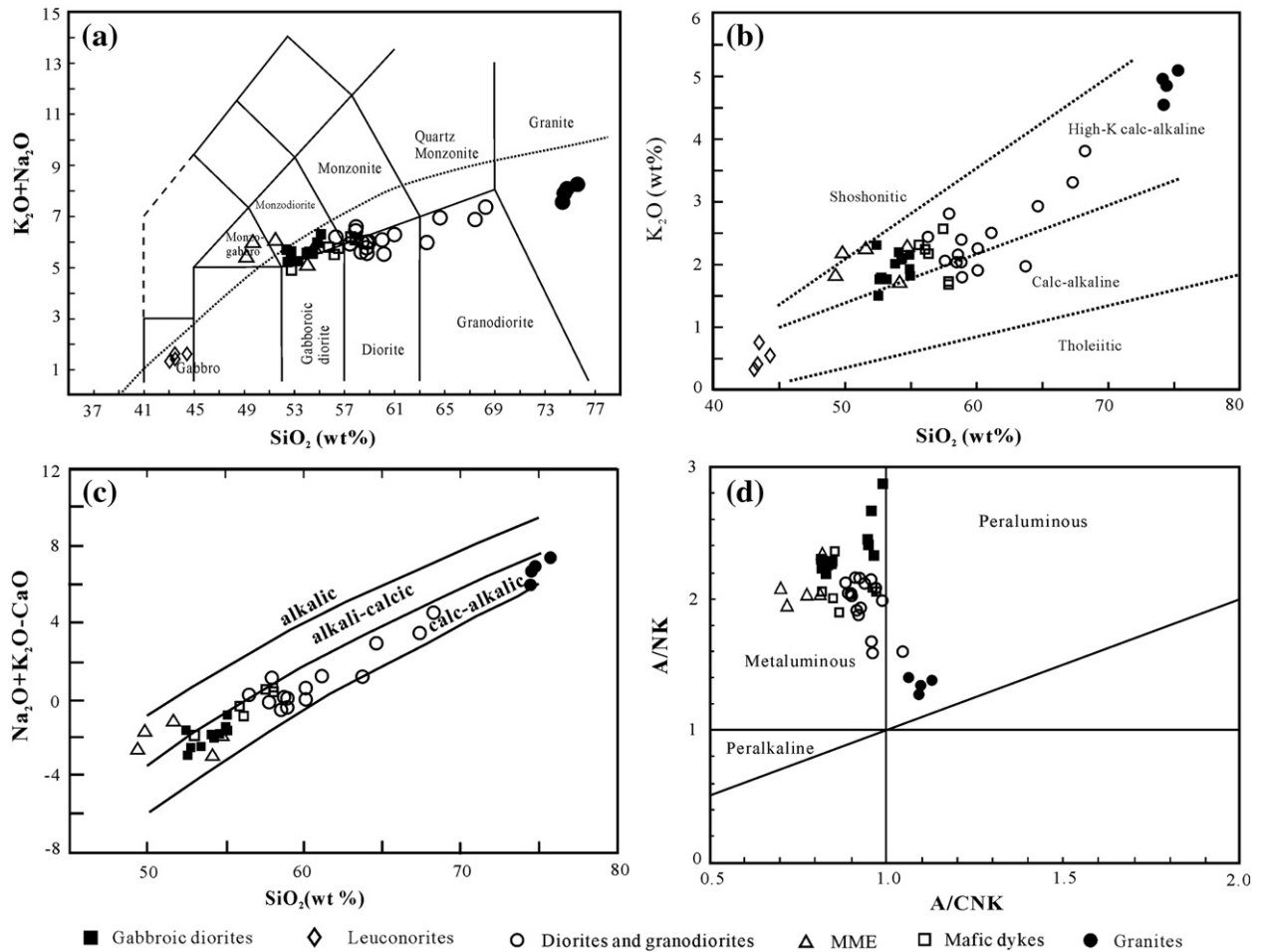


Fig. 6. Classification diagrams for the various rock types in the Guyang batholith. (a) Total alkalis vs. silica (Le maitre, 2002). (b) Plot of K_2O vs. SiO_2 . (c) Plot of $(Na_2O + K_2O - CaO)$ vs. SiO_2 (Frost et al., 2001). (d) Plot of A/NK vs. A/CNK [A/NK = molar ratio of $Al_2O_3/(Na_2O + K_2O)$; A/CNK = molar ratio of $Al_2O_3/(CaO + Na_2O + K_2O)$].

5.5. Zircon Hf isotopes

As presented in the Online Supplemental Table 5 and Fig. 11, zircons from sample NM07-56 show a range of initial $^{176}Hf/^{177}Hf$ ratios from 0.28233 to 0.28241 and $\epsilon_{Hf}(t)$ values from -6.7 to -9.6 , with crustal model ages (T_{DM}) of 1744 to 1908 Ma. Zircons from sample NM07-73 exhibit a range of initial $^{176}Hf/^{177}Hf$ ratios from 0.28226 to 0.28232, $\epsilon_{Hf}(t)$ values from -9.8 to -12.0 and model ages between 1908 and 2056 Ma. Zircons from sample NM07-144 display a range of initial $^{176}Hf/^{177}Hf$ ratios from 0.28210 to 0.28227 and $\epsilon_{Hf}(t)$ values from -11.6 to -15.5 . The Hf model ages (T_{DM}) for these zircons mainly range between 2032 and 2419 Ma. Zircons from sample NM07-145 show a range of initial $^{176}Hf/^{177}Hf$ ratios from 0.28218 to 0.28235, $\epsilon_{Hf}(t)$ values from -8.8 to -14.7 , and model ages between 1858 and 2224 Ma. Zircons from sample NM07-181 have initial $^{176}Hf/^{177}Hf$ ratios ranging from 0.28228 to 0.28237, $\epsilon_{Hf}(t)$ values from -7.9 to -11.1 , and model ages between 1802 and 2002 Ma. Zircons from sample NM07-156 show a range of initial $^{176}Hf/^{177}Hf$ ratios from 0.28218 to 0.28235, $\epsilon_{Hf}(t)$ values from -8.8 to -14.7 , and model ages between 1840 and 2047 Ma.

6. Conditions of crystallization

For the gabbroic rocks, applying the two-pyroxene thermometer of Taylor (1998) yields estimated equilibration temperatures of 842–909 °C for a reasonable pressure of 5 kbar, while using that of Wells (1977) gives temperatures between 874 and 911 °C. The concordance between two methods suggests that they crystallized from a high-T (>900 °C) mantle-sourced magma.

As reviewed by Anderson et al. (2008), the combined use of the hornblende–plagioclase thermometer of Holland and Blundy (1994) and the Anderson and Smith (1995) calibration of the Al-in-hornblende barometer can yield more precise P–T estimates from other thermobarometers for granitic systems. In our case, the condition for their application is fully satisfied by the typical mineral assemblage quartz + plagioclase + orthoclase + hornblende + biotite + titanite + magnetite + apatite in some diorite–granodiorite and MME. As shown in the Online Supplemental Table 6, the calculated temperatures and pressures are 684–821 °C and 2.55–4.52 kbar, respectively. This is not only consistent with the presence of magmatic epidote, which commonly denotes pressure above 2.1 to 2.80 ± 0.5 kbar (Vyhnal et al., 1991), but is also in agreement with the zircon saturation temperatures of 708–778 °C for the diorite and granodiorite. Assuming an average crustal density of 3.0 g cm^{-3} , this pressure range corresponds to a depth of about 8.5 to 16.8 km (average 12 km). For the granitic rocks, Zr abundances in them result in zircon saturation temperatures of 708–738 °C. This temperature range should be considerably lower than the temperature of the intruding magma due to the late crystallization of zircon.

7. Discussion

7.1. Early Permian giant igneous event

The high-quality zircon U–Pb and hornblende Ar^{40}/Ar^{39} chronological data presented above, firmly established an emplacement time of Early Permian for various lithologies of the Hercynian Guyang batholith. Coeval

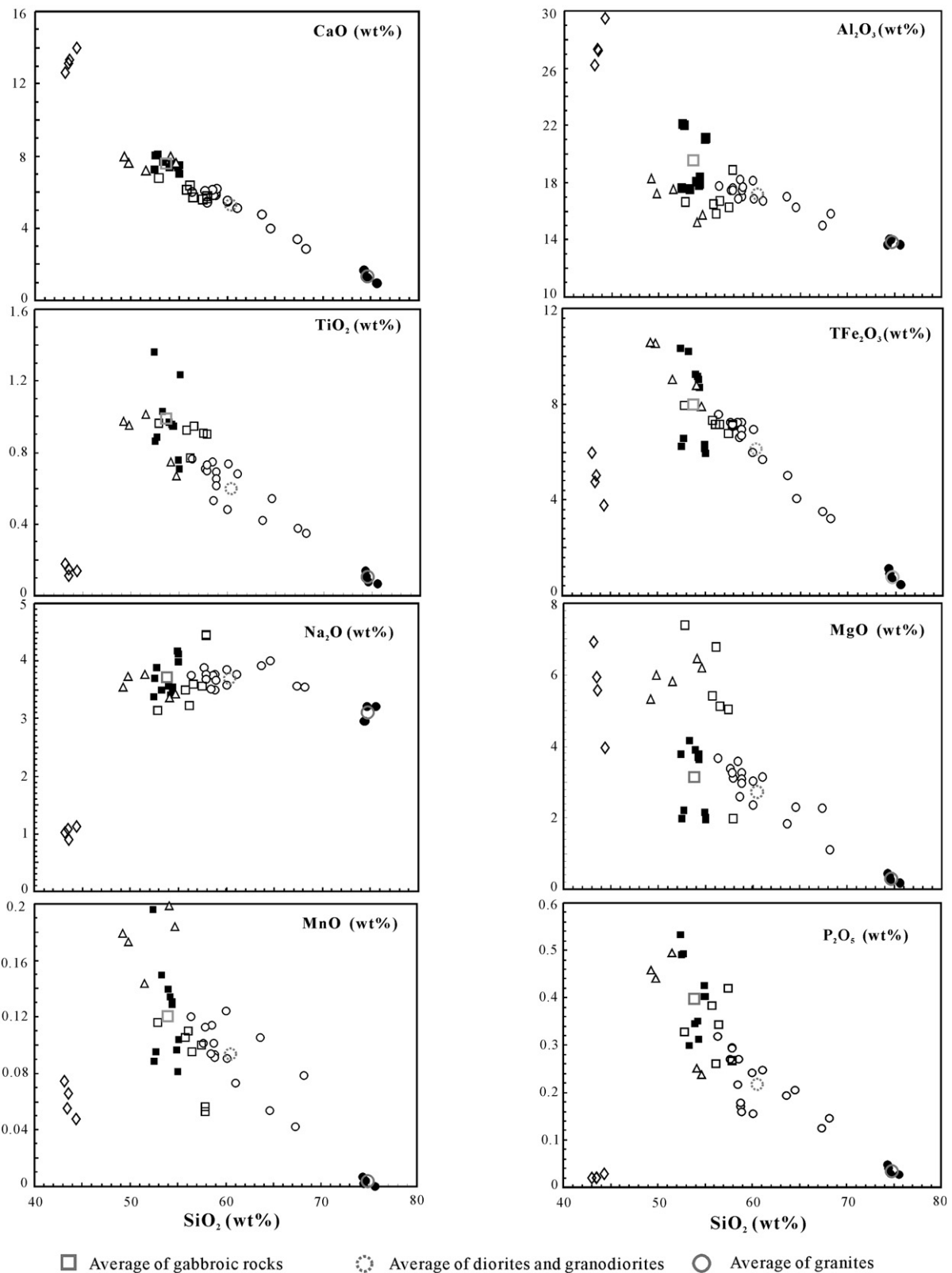


Fig. 7. Plots of oxides vs. SiO₂ for the various rock types in the Guyang batholith. Symbols are the same as in Fig. 6.

igneous rocks are also widely recognized by recent geochronological studies from the neighboring areas (Fig. 1c). At Wulatezhongqi to the near west, SHRIMP zircon U–Pb dating yielded ages of 291 ± 3 Ma for the diorite stock (Luo et al., 2007), 277 ± 3 Ma for the A-type granitic batholith and 277 Ma for the gabbro stock (Luo et al., 2009), respectively. At Dongshenmiaoy, the peraluminous S-type granites have been dated at

286–276 Ma by the monazite U–Th–Pb method (Luo et al., 2009). At Bayan Obo to the nearest north, the mafic–ultramafic rocks have been constrained to be formed during the period of 285 to 256 Ma by SHRIMP zircon U–Pb method (Luo et al., 2009), while the diorite–granodiorite–granite series has been dated at 281–263 Ma by the LA–ICPMS method (Fan et al., 2009). At Xianghuangqi to the east, LA–ICPMS zircon dating

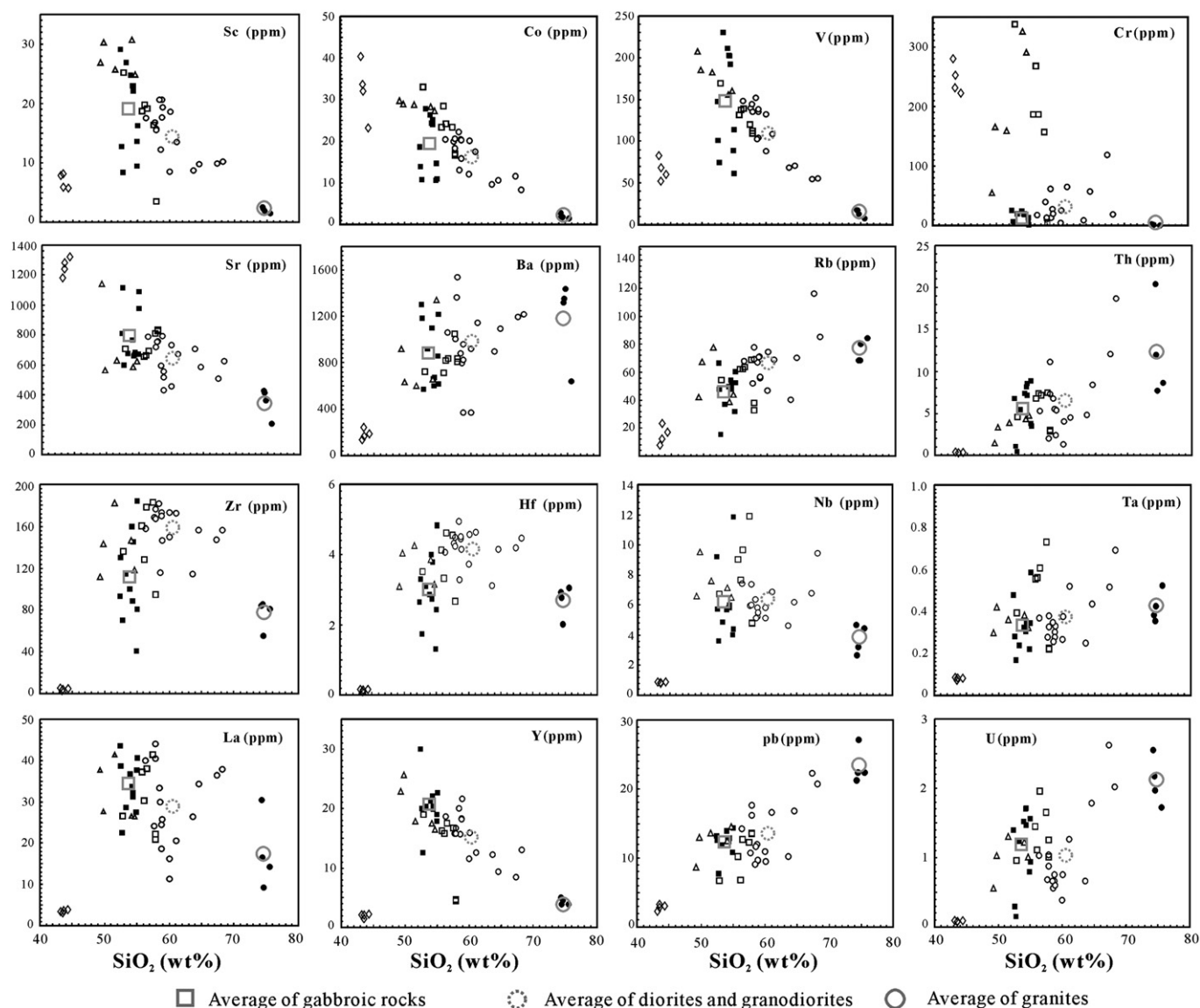


Fig. 8. Plots of various trace elements vs. SiO₂ for the various rock types in the Guyang batholith. Symbols are the same as in Fig. 6.

gave an age of 271 ± 3 Ma for the granite-porphry (Lu et al., 2009), while the TIMS dating yielded ages from 275 to 262 Ma for the peraluminous S-type granites (Hong et al., 2007).

Early Permian intrusive rocks are also frequent in other regions of the northern NCC. At the northern Hebei along its middle segment, zircon U–Pb dating revealed a series of gabbro–diorite–granodiorite plutons with ages between 290 Ma and 275 Ma (Chen et al., 2009b; Zhang et al., 2009a,b). The peraluminous S-type granites have been dated at 281–252 Ma by the monazite U–Th–Pb method (Wang et al., 2007a). Much further east at the northern Liaoning and southern Jilin provinces, SHRIMP zircon dating recognized several Early Permian granitic rocks from the previously-regarded Precambrian basement (Zhang et al., 2004, 2005).

Early Permian magmatic rocks are also widely distributed beyond the northern margin of the NCC. To its north in the Inner Mongolian part of the CAOB, the volcanic rocks constitute dominant components of the Lower Permian lithological sequence. Recent zircon U–Pb dating established an eruption time of ca. 280 Ma for the bimodal volcanic rocks from central Inner Mongolia (Zhang et al., 2008) and 289–287 Ma for the high-K calc-alkaline volcanic rocks from north-western Inner Mongolia (Zhang et al., 2011). For various intrusive rocks, zircon U–Pb dating yielded ages of 286 to 276 Ma for the A-type

granites (Shi et al., 2004; Zhang and Zhai, 2010), 282 to 260 Ma for the granodiorites and 281 Ma for the peraluminous S-type granites at Dongwuqi (Bao et al., 2007).

Early Permian igneous rocks are not just limited to the territory of China. In the southern Mongolian segment of the CAOB bordering on China, the Khan Bogd pluton, one of the world's largest alkali granites (over 1500 km²), has been dated at 291–283 Ma by TIMS zircon U–Pb and hornblende ⁴⁰Ar/³⁹Ar methods (Kovalenko et al., 2006). TIMS zircon U–Pb dating also yielded ages of 292 ± 1 Ma for the alkali granites of the Mandakh Massif and 284 ± 1 Ma for the alkaline granites of the Abdarakit Massif (Yarmolyuk et al., 2008), respectively.

In summary, it seems clear that there occurred a giant Early Permian igneous event over the vast area of the northern China–Mongolia tract (Fig. 1c; Zhang and Zhai, 2010). It features a wide range of plutonic rock types, including dominant medium- to high-K calc-alkaline granitoids, subordinate peraluminous S-type and alkaline–peralkaline A-type granites, and minor but sporadic mafic–ultramafic rocks.

7.2. Petrogenesis

The Guyang batholith, with its mafic components showing a magnesian-potassic affinity and its felsic ones displaying a high-K

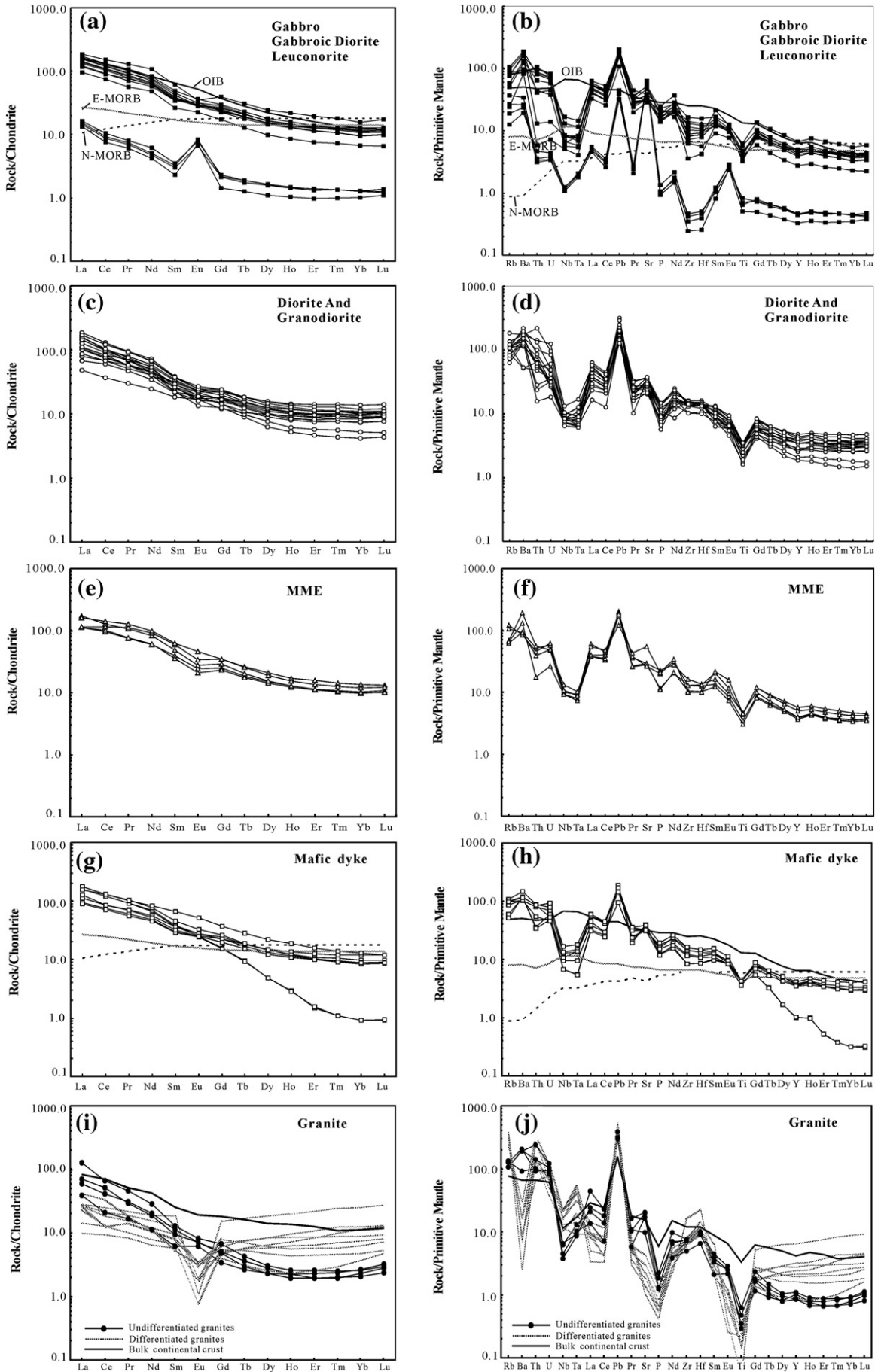


Table 2
Rb–Sr and Sm–Nd isotopic compositions for the various rock types of the Guyang batholith.

Sample no.	Rock type	Rb (ppm)	Sr (ppm)	⁸⁷ Rb/ ⁸⁶ Sr	⁸⁷ Sr/ ⁸⁶ Sr	±2σ	(⁸⁷ Sr/ ⁸⁶ Sr) _t	Sm (ppm)	Nd (ppm)	¹⁴⁷ Sm/ ¹⁴⁴ Nd	¹⁴³ Nd/ ¹⁴⁴ Nd	±2σ	Initial Nd	ε _{Nd} (280 Ma)	T _{DM} (Ma)
NM56	G.D	52.36	672.9	0.2252	0.705941	0.000011	0.70504	5.737	29.58	0.1173	0.512069	0.000013	0.511854	−8.27	1705
NM58	G.D	35.92	695.3	0.1495	0.705657	0.000011	0.70506	5.108	24.96	0.1237	0.512054	0.000014	0.511827	−8.79	1851
NM59	G.D	50.79	687.2	0.2139	0.705890	0.000010	0.70504	4.648	24.02	0.1170	0.512078	0.000017	0.511864	−8.08	1686
NM62	G.D	44.98	772.8	0.1684	0.705821	0.000011	0.70515	5.406	28.33	0.1154	0.512043	0.000012	0.511831	−8.71	1712
NM67	L	6.320	1188	0.0154	0.704658	0.000011	0.70460	0.459	2.354	0.1179	0.512097	0.000012	0.511881	−7.74	1672
NM68	L	20.60	1326	0.0450	0.704783	0.000013	0.70460	0.755	3.852	0.1185	0.512094	0.000016	0.511877	−7.82	1687
NM71	L	15.13	1567	0.0280	0.704735	0.000010	0.70462	0.801	4.143	0.1168	0.512096	0.000016	0.511882	−7.73	1654
NM73	G.a	55.16	977.6	0.1633	0.705917	0.000010	0.70527	6.788	36.36	0.1129	0.511985	0.000013	0.511778	−9.75	1757
NM74	G.D	39.05	953.5	0.1185	0.705795	0.000011	0.70532	6.773	35.68	0.1148	0.511981	0.000012	0.511771	−9.90	1797
NM79	Ga	24.55	1051	0.0676	0.705468	0.000012	0.70520	6.414	34.39	0.1128	0.511961	0.000015	0.511754	−10.2	1791
NM86	Dyke	59.66	651.2	0.2652	0.706743	0.000011	0.705686	5.860	32.78	0.1081	0.512080	0.000018	0.511882	−7.73	1542
NM88	Dyke	33.63	808.5	0.1204	0.706016	0.000010	0.705536	4.569	23.25	0.1188	0.512024	0.000015	0.511806	−9.2	1804
NM94	Dyke	28.81	805.2	0.1035	0.705977	0.000011	0.705565	4.161	20.88	0.1205	0.512019	0.000013	0.511798	−9.36	1844
NM96	D	66.36	515.2	0.3728	0.706910	0.000011	0.705425	4.024	19.56	0.1244	0.511798	0.000010	0.511570	−13.81	2298
NM97	D	60.24	518.8	0.3360	0.706568	0.000011	0.705229	4.715	24.33	0.1171	0.511787	0.000015	0.511572	−13.77	2142
NM100	D	78.00	448.3	0.5036	0.707290	0.000012	0.705284	3.602	17.03	0.1278	0.511802	0.000014	0.511568	−13.86	2381
NM108	G.D.R	102.3	472.4	0.6271	0.708886	0.000009	0.706388	3.253	20.89	0.0942	0.511758	0.000014	0.511585	−13.51	1771
NM138	Dyke	48.62	672.2	0.2093	0.706270	0.000010	0.705436	5.125	25.88	0.1197	0.512258	0.000015	0.512039	−4.67	1444
NM143	D	61.00	567.4	0.3111	0.706258	0.000011	0.705019	4.771	25.63	0.1126	0.511773	0.000012	0.511567	−13.88	2069
NM144	D	48.19	703.0	0.1984	0.706158	0.000011	0.705368	4.218	21.13	0.1207	0.511913	0.000011	0.511692	−11.44	2020
NM145-1	MME	35.96	566.6	0.1837	0.706391	0.000010	0.705659	4.966	24.66	0.1217	0.511996	0.000014	0.511773	−9.85	1906
NM145-3	MME	77.18	626.3	0.3567	0.707028	0.000012	0.705607	6.573	36.62	0.1085	0.511958	0.000012	0.511759	−10.12	1723
NM146	G.D.R	68.00	675.2	0.2915	0.706751	0.000012	0.70559	3.931	20.17	0.1178	0.511963	0.000013	0.511747	−10.36	1881
NM151	MME	67.93	597.8	0.3289	0.706907	0.000011	0.705597	8.214	41.21	0.1205	0.511981	0.000013	0.511760	−10.1	1906
NM152	D	79.05	616.8	0.3710	0.707625	0.000015	0.706147	3.091	19.42	0.0962	0.511822	0.000011	0.511646	−12.34	1718
NM156	G	69.8	426.0	0.4743	0.707188	0.000012	0.705298	1.73	12.4	0.0843	0.511893	0.000012	0.511738	−10.52	1478
NM159	MME	37.83	1112	0.0985	0.705331	0.000010	0.704939	8.795	46.26	0.1150	0.512054	0.000011	0.511843	−8.48	1689
NM162	G	75.6	453.7	0.4822	0.707449	0.000012	0.705528	1.48	9.88	0.0904	0.511886	0.000010	0.511720	−10.88	1560
NM167	D	90.83	646.9	0.4064	0.706611	0.000012	0.704992	4.003	24.15	0.1002	0.511944	0.000011	0.511760	−10.1	1616
NM168	G	101.9	235.1	1.2554	0.710298	0.000013	0.705297	1.72	10.1	0.1035	0.511888	0.000009	0.511698	−11.31	1741
NM181	D	73.70	713.5	0.2989	0.706795	0.000013	0.705604	5.403	30.33	0.1077	0.512047	0.000012	0.511850	−8.36	1583

Notes: $(^{87}\text{Sr}/^{86}\text{Sr})_t = (^{87}\text{Sr}/^{86}\text{Sr})_{\text{sample}} - (^{87}\text{Rb}/^{86}\text{Sr})_{\text{sample}} \times (e^{\lambda t} - 1)$, $\lambda = 1.42 \times 10^{-11} \text{ year}^{-1}$ (Steiger and Jäger, 1977); initial Nd = $(^{143}\text{Nd}/^{144}\text{Nd})_{\text{sample}} - (^{147}\text{Sm}/^{144}\text{Nd})_{\text{sample}} \times (e^{\lambda t} - 1)$, $\epsilon_{\text{Nd}} = ((^{143}\text{Nd}/^{144}\text{Nd})_{\text{sample}} / (^{143}\text{Nd}/^{144}\text{Nd})_{\text{CHUR}} - 1) \times 10,000$, $f_{\text{Sm}/\text{Nd}} = (^{147}\text{Sm}/^{144}\text{Nd})_{\text{sample}} / (^{147}\text{Sm}/^{144}\text{Nd})_{\text{CHUR}} - 1$, $T_{\text{DM}} = 1 / \lambda \times \ln(1 + ((^{143}\text{Nd}/^{144}\text{Nd})_{\text{sample}} - 0.51315) / ((^{147}\text{Sm}/^{144}\text{Nd})_{\text{sample}} - 0.2137))$, where $(^{147}\text{Sm}/^{144}\text{Nd})_{\text{CHUR}} = 0.1967$, $(^{143}\text{Nd}/^{144}\text{Nd})_{\text{CHUR}} = 0.512638$, $\lambda_{\text{Sm}} = 6.54 \times 10^{-12} \text{ year}^{-1}$ (Lugmair and Marti, 1978).

calc-alkaline character, is similar to numerous medium- to high-K calc-alkaline mafic–felsic igneous associations worldwide (e.g., Barbarin, 2005; Bonin, 2004). Likewise, experimental arguments, field evidence, petrographic and geochemical data for these coexisting mafic and felsic suites suggest that their genesis may involve a complex interplay of several petrogenetic processes, including contemporaneous melting of distinct mafic and felsic sources, and subsequent episodic mafic–felsic magma interactions. To unravel this complex petrogenetic scenario, the first step is to constrain the end-members of this mafic–felsic system.

7.2.1. Mafic magma sources

As opposed to the basaltic rocks, the identification of the original melt for gabbroic rocks often poses particular difficulties due to the complicated effects from fractional crystallization, mineral accumulation and crustal assimilation. For the gabbro and gabbroic diorite samples from the YHY stock, their rather low silica contents and restricted isotopic compositions indicate that they seem to be exempt from any significant effects of fractional crystallization and crustal assimilation. Furthermore, the MgO, Cr and Ni contents in these samples are far below those expected for the rocks with a cumulate origin (MgO > 15%, Cr > 2000 ppm, and Ni > 300 ppm) (e.g., Roberts et al., 2000). In addition, it is clear that there exists close resemblance in trace element patterns between these rocks and the mafic dykes that have an inherent liquid affinity (Fig. 8). Therefore, these less-differentiated gabbroic rocks, together with some primitive samples from massive mafic dykes with obvious chilled margins, are most likely to have a

composition closest to the parental basaltic melt in terms of elemental and isotopic compositions.

In regard to trace element, these rocks are characterized by selective enrichment of LILE, U, Pb and light REE, and depletion in HFSE (e.g., Nb, Ta and Ti), thus resulting in high values of La/Nb (3.4–8.5), Ba/Nb (102–212), and Zr/Nb ratios (10–27) and low Ce/Pb (4.7–7.2). These values are closely similar to those of arc volcanic rocks worldwide (e.g., Stern, 2002). Such geochemical features can be ascribed either to partial melting of an enriched mantle source that was previously enriched in LILE and LREE by slab-derived hydrous fluids or melts prior to magma generation, or to extensive crustal contamination of MORB-like magmas during their emplacement (Zhang et al., 2010b).

With respect to isotopic data, the marked crustal signatures evidenced by moderately negative ε_{Nd}(t) and zircon ε_{Hf}(t) values in these mafic rocks seem to be at odds with the relatively refractory character of the sub-continental lithospheric mantle beneath the northern NCC during Early Paleozoic times, as constrained by the perovskite grains from the Ordovician kimberlites (Yang et al., 2009) and the Middle Devonian mafic–ultramafic rocks from the northern NCC (Zhang et al., 2009d) (Figs. 10 and 11). Specifically, the former yield uniform Sr and Nd isotopic compositions with an average ⁸⁷Sr/⁸⁶Sr_i ratio of ca. 0.7037 and ε_{Nd}(t) values of −0.36 to +1.66 (Yang et al., 2009), while relatively uncontaminated samples from the latter give a restricted range of isotopic compositions with ⁸⁷Sr/⁸⁶Sr_i of ca. 0.7046 and ε_{Nd}(t) of −1.5 to −4 (Zhang et al., 2009d). Considering the likely tectonic scenario of the northern NCC at that time, the isotopic

Fig. 9. Chondrite-normalized REE patterns (a), (c), (e), (g), and (i) and primitive mantle-normalized trace element spidergrams (b), (d), (f), (h), and (j) for the gabbro–gabbroic diorite–leuconorite, diorite and granodiorite, MME, mafic dyke and monzogranite, respectively, from the Guyang batholith. Data for the highly-differentiated granites are from our unpublished data in the Online Supplement Table 8. Normalization values are from Sun and McDonough (1989). The data for oceanic island basalt (OIB), normal mid-ocean ridge basalt (N-MORB) and enriched mid-ocean ridge basalt (E-MORB) are also from Sun and McDonough (1989). Bulk continental crust data are from Rudnick and Gao (2003).

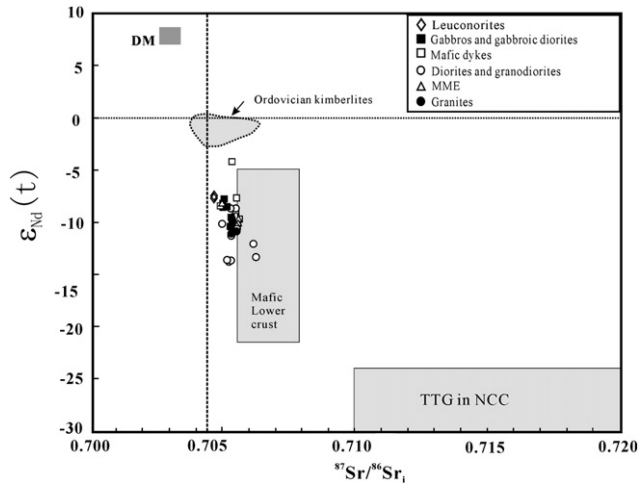


Fig. 10. Plot of initial $\epsilon_{Nd}(t)$ and $^{87}Sr/^{86}Sr_1$ for various rock types in the Guyang batholith. The field for the Ordovician kimberlites rocks from the North China Craton is from Yang et al. (2009). Mafic lower crust and TTG gneisses in the North China Craton are from Jahn et al. (1987), Zhou et al. (2002), Liu et al. (2004), Chen et al. (2009b).

enrichment in our mafic rocks can be attributed either to reactions between mantle wedge and slab-derived hydrous fluids or melts during the subduction that led to the Early Devonian amalgamation between the NCC and the Bainaimiao arc terrane (Zhang et al., 2010a), or to extensive crustal contamination during magma ascent. Alternatively, such enriched signature may reflect the long-lasting memory of ancient subduction processes in the lithospheric mantle, as evidenced by the Archean to Paleoproterozoic Nd model ages for multiple episodes of the Paleozoic mantle-derived magmatic rocks from the northern NCC (this study, Zhang et al., 2009a,b,d, 2010a) and by the recent documentation of the Paleoproterozoic ridge-subduction event in the region (Peng et al., 2010).

The present mafic rocks have much higher Sr abundance (684–1116 ppm) than that of continental crust in general ($Sr=280\text{--}348$ ppm; Rudnick and Gao, 2003) and local upper crust country rocks (25–100 ppm) as represented by the meta-sedimentary rocks of the Zhaertai group (Li et al., 2007). They also display distinct Sr–Nd isotopic compositions ($^{87}Sr/^{86}Sr_1=0.7053\text{--}0.7056$, $\epsilon_{Nd}(t)=-7.73$ to -10.2) from those ($^{87}Sr/^{86}Sr_1=0.710\text{--}0.730$, $\epsilon_{Nd}(t)=-25$ to -43) of the Archean TTG gneiss-like lower crustal component of the NCC (Chen et al., 2009b; Jahn et al., 1987). This argues against such potential basement or wallrock assimilants as the source of the

enrichments observed in these rocks. However, the Archean mafic lower crust in the NCC, with its relatively low $^{87}Sr/^{86}Sr$ ratios (mostly 0.7055–0.708) and highly varied ϵ_{Nd} values (mostly in the range of -5 to -22) (Jahn et al., 1987; Liu et al., 2004; Zhou et al., 2002), seems to be a feasible contaminant. Nevertheless, the restricted Sr–Nd range shown by most of our samples conforms well to that ($^{87}Sr/^{86}Sr_1=0.7052$, $\epsilon_{Nd}(t)=-8$) of the enriched mantle in the NCC during Early Permian time as constrained by lamprophyres and olivine gabbros (Chen et al., 2009b). These features, together with the lack of any systematic correlated variations of $^{87}Sr/^{86}Sr_1$ and $\epsilon_{Nd}(t)$ with SiO_2 (Fig. 12), seem to exclude mafic lower crust from having played any significant role in their genesis. Therefore, we assert that the arc-type geochemical signatures and the evolved isotopic compositions in our mafic rocks are more consistent with a wet, subduction-related metasomatized sub-continental lithospheric mantle (SCLM) than a convecting asthenosphere. So does the presence of primary hornblende and biotite (McMillan et al., 2003).

For the transport of trace elements in the mantle wedge, the prevailing model is that different types of metasomatic agents (e.g., fluid, silicic or carbonatite melt) could yield distinctive trace element and isotopic imprints in metasomatized mantle (e.g., Menzies, 1987). Specifically, slab-derived fluids usually carry significant amounts of Si and LILE to the mantle wedge to the shallower depths (e.g., Plank and Langmuir, 1993; Stein et al., 1997), whereas slab melts may be the metasomatic agents at greater depths (Killian and Stern, 2002; Rapp et al., 1999) and produce more sodic metasomatic products. This could result in the fractionation of selected element pairs such as Ba/La, Th/La, Pb/La or Nb/Y, since Th and LREE are thought to be less mobile in aqueous fluids than the LILE, U and Pb (McCulloch and Gamble, 1991; Pearce et al., 1999). Consequently, these variables can serve as reliable indicators of potential sediment or fluid contributions from the subducted slab to magma source regions (Woodhead, et al., 2001). In our case, high Ba/La and Th/Ta ratios in the mafic rocks may reflect potential dual inputs of slab-derived fluids and sediment-derived hydrous melts (Fig. 13a), while high $(Hf/Sm)_{PM}$ and low $(Ta/La)_{PM}$ ratios point to a fluid-dominated subduction metasomatism (Fig. 13b).

With these subduction-related trace elemental and enriched isotopic features, the present mafic rocks are similar to numerous coeval analogs from the neighboring regions of the northern NCC, such as the Early Permian Gaositai Alaskan-type ultramafic complex (Chen et al., 2009b) and other mafic-ultramafic complexes from the eastern Hebei province (Zhang et al., 2009d). These analogs are interpreted to have an origin consistent with partial melting of a metasomatized lithospheric mantle (Chen et al., 2009b; Zhang et al., 2009d). Therefore, it follows that an enriched SCLM seems to be a

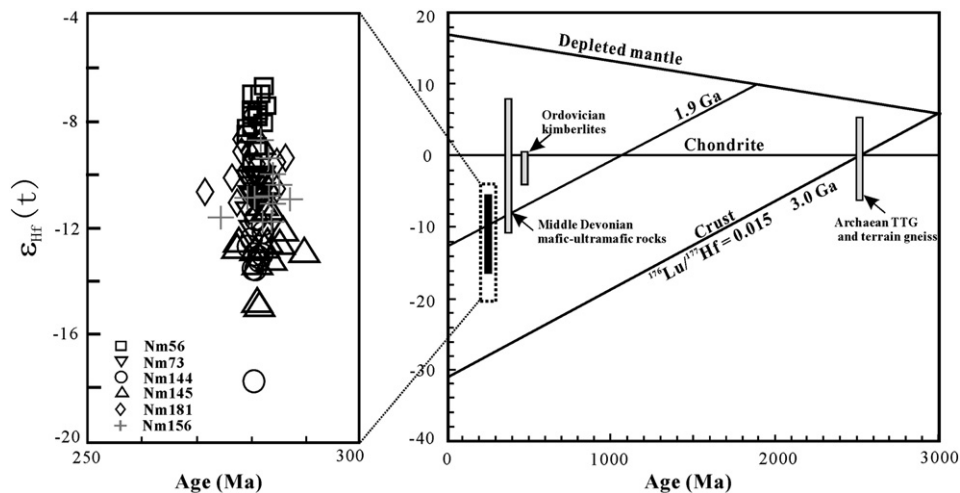


Fig. 11. $\epsilon_{Hf}(t)$ vs. U–Pb age plot for zircons from various rock types in the Guyang batholith. Also shown for comparison is the Hf isotopic evolution line of the Archean average crust with $f_{Lu/Hf}=0.015$ (Griffin et al., 2002).

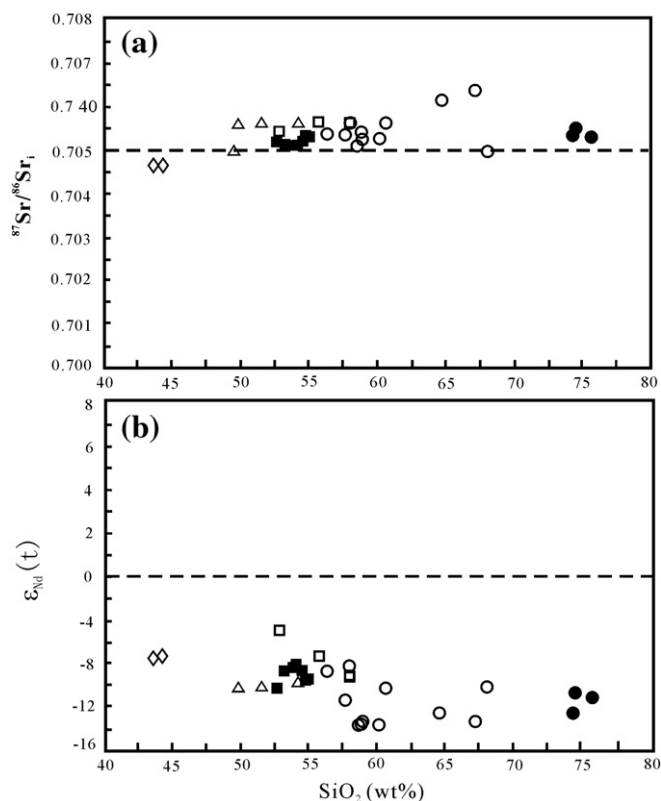


Fig. 12. Plots of (a) $^{87}\text{Sr}/^{86}\text{Sr}_1$ vs. SiO_2 and (b) $\epsilon_{\text{Nd}}(t)$ vs. SiO_2 .

consistent source for the mafic magma end-member in the genesis of the granitoid batholith in the northern NCC.

7.2.2. Felsic magma sources

As shown above, the monzogranites exhibit high alkali contents, low CaO and P_2O_5 , elevated Ba and Sr, and low abundances of Nb and Ta. These are typical of major and trace element geochemical features of undifferentiated high-K calc-alkaline I-type magmas (Barbarin, 1999; Landenberger and Collins, 1996). Furthermore, they bear a remarkable geochemical resemblance to the high-silica adakites (Moyen, 2009), such as low abundances of garnet-compatible elements (Y and HREE), high contents of plagioclase-compatible Sr and Ba, high ratios of Sr/Y and La_N/Yb_N and absence of significant Eu anomalies.

As critically reviewed by Moyen (2009), such high Sr/Y felsic magmas can be attributed to various petrogenetic scenarios, including (1) partial melting of subducted oceanic crust and subsequent interaction of the melts with the overlying mantle wedge (Defant and Drummond, 1990); (2) assimilation and fractional crystallization (AFC) involving a mantle-derived basaltic magma (Castillo et al., 1999; Macpherson et al., 2006); and (3) partial melting of a high Sr/Y (and La/Yb) source such as the mafic lower arc crust (Atherton and Petford, 1993; Rapp et al., 2002, 2003; Xiao and Clemens, 2006) or mafic lower continental crust (Gao et al., 2004; Jiang et al., 2007; Wang et al., 2007b).

For the present monzogranites, their moderately enriched Sr–Nd–Hf_{Zircon} isotopic compositions preclude the possibility of slab melting in conjunction with melt–peridotite interaction. Experimental data on MORB-like compositions suggest that the resultant partial melts at pressures between 1 and 2 GPa and temperatures of $\leq 1000^\circ\text{C}$ are generally characterized by low K_2O (mostly $< 1.2\text{ wt.}\%$) and $\text{K}_2\text{O}/\text{Na}_2\text{O}$ ratios (mostly < 0.25), regardless of the amount of H_2O present in the system (López and Castro, 2001; Rapp and Watson, 1995).

Given the coexistence of the coeval mafic to intermediate rocks, it is tempting to ascribe the genesis of these granites to extreme differen-

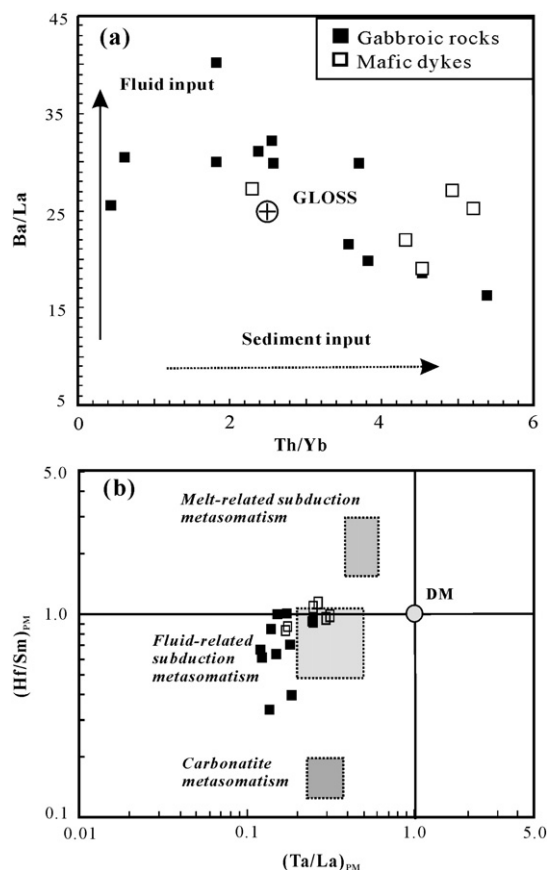


Fig. 13. (a) Ba/La vs. Th/Yb and (b) $(\text{Ta}/\text{La})_{\text{PM}}$ vs. $(\text{Hf}/\text{Sm})_{\text{PM}}$ plots for the mafic rocks from the Guyang batholith. In (a), continuous vector, slab-derived fluids; dashed vector, sediment input in the source as represented and discussed by Woodhead et al. (2001). Global subducting sediment (GLOSS) compositions are from Plank and Langmuir (1993). In (b), 'PM' denotes the values normalized to the primitive mantle; the fields of the subduction and carbonatite-related metasomatism are from La Flèche et al. (1998).

tiation. However, several arguments are against this possibility. First, field relationships (IMBGMR, 1972) and the present high-precision ages constrain that the granites predated, albeit slightly, the mafic and intermediate ones. Second, with plagioclase as a liquidus phase in the granites as indicated by the petrography, any prior crystal fractionation would have considerably increased Ca/Sr and Rb/Sr ratios. However, the present samples turned out to have Ca/Sr ratios of 21 to 34, Rb/Sr ratios of 0.16 to 0.41, Rb/Ba ratios of 0.06 to 0.13, and K/Ba ratios of 28 to 66, respectively. These comparable ratios to those of parental magmas for typical I-type granites (Landenberger and Collins, 1996; Zhang et al., 2011) attest to minimal prior fractionation of plagioclase. Third, the granitic melts in the situation of extreme differentiation should be characterized by strong enrichment in many HFSE due to their incompatible behavior, and by large negative Eu anomalies resulting from fractionation of plagioclase. They generally develop consistent chondrite-normalized REE patterns with a concave-upward shape, as exemplified in the coeval (278 Ma, our unpublished data in the Online Supplemental Table 7) highly-differentiated granites from the study area (Fig. 9i, our unpublished data in the Online Supplemental Table 8). The chemistry of the monzogranites herein contrasts markedly with these trends. Fourth, most granite samples have lower initial $^{87}\text{Sr}/^{86}\text{Sr}$ ratios and more depleted Nd composition than some intermediate facies rocks. This appears to be inconsistent with what might be expected in the case of an AFC process.

As such, partial melting of a high-K mafic lower crustal source seems necessary to accommodate the mineralogy and geochemical characteristics of these adakitic granites, as shown from numerous experimental (e.g. Rapp et al., 2002; Sisson et al., 2005; Xiao and Clemens, 2006) and

geochemical case studies (Jiang et al., 2007; Wang et al., 2007b; Zhang et al., 2011). The application of this model to the present monzogranites is consistent with (1) their high Sr and Ba contents, suggesting a plagioclase-free source; (2) the concave-upward REE patterns and lack of Eu anomalies, implying the predominance of residual amphibole in the source.

In terms of isotopic signature, the monzogranites have evolved whole-rock Sr–Nd and zircon Hf isotopic compositions with $^{87}\text{Sr}/^{86}\text{Sr}_i$ of 0.7053 to 0.7055, $\varepsilon_{\text{Nd}}(t)$ values of -10.5 to -11.3 and zircon $\varepsilon_{\text{Hf}}(t)$ values of -8.8 to -14.7 . These isotopic variations are not only largely indistinguishable from those of the coeval gabbroic to granodioritic rocks (Fig. 12), but also resemble those of the Archean mafic lower crust in the northern NCC, which has been constrained to have relatively low $^{87}\text{Sr}/^{86}\text{Sr}$ ratios (mostly 0.7055–0.708) and highly varied ε_{Nd} values (mostly in the range of -5 to -22) (Jahn et al., 1987; Liu et al., 2004; Zhou et al., 2002). Distinguishing these two candidate protoliths is not easy. Given the small but significant degree of isotope heterogeneity among the granite and some granodiorite samples, plus their Late Paleoproterozoic Nd and zircon Hf model ages, the most likely scenario is that the felsic magmas were produced by melting of a mixed lithology containing a dominant newly underplated mafic lower crust component and a minor ancient mafic lower crust component.

7.2.3. Hybridized nature of the diorites and granodiorites

As shown above, the diorites and granodiorites show various scales of field and petrographic textures, such as meter-sized MME (Fig. 2a), centimeter-sized mafic mineral clots, complexly zoned plagioclase (Fig. 2c and d), millimetric hornblende-mantled quartz ocelli. These features indicate that intensive mass transfer between mafic magma and still unconsolidated felsic host magma seems to be the rule rather than the exception in the formation of diorites and granodiorites. As is widely accepted, MME commonly represent the final products from the complex physico-chemical process experienced by mafic magmas injected into the host felsic magmas (Barbarin, 2005; Bonin, 2004; Poli and Tommasini, 1991, 1999). The hornblende-mantled quartz ocelli are widely documented in the hybrid granitoids worldwide to typify micro-scale textural evidence for magma hybridization (Hibbard, 1991; Vernon, 1991). The present consensus for their origin is that quartz crystals from the felsic system came in contact with the liquid phase of the mafic magma and promoted the nucleation of fine-grained hornblende on their rims (Hibbard, 1991; Renna et al., 2006; Vernon, 1991). Complex zoning in plagioclase can be interpreted to indicate that plagioclase crystals migrated between variably mixed mafic and felsic environments during their crystallization (Janoušek et al., 2004; Słaby and Martin, 2008).

The nature of mafic–felsic magma interaction can be further testified by their geochemical data. On $\text{Al}_2\text{O}_3/(\text{K}_2\text{O} + \text{Na}_2\text{O})$ vs. $\text{Al}_2\text{O}_3/(\text{CaO} + \text{K}_2\text{O} + \text{Na}_2\text{O})$ (Fig. 6d), with the exception of the leuconorite samples, the diorite and granodiorite define a linear trend linking the monzogranite and gabbroic rocks. As in the case of the Hercynian Karkoosze pluton (Słaby and Martin, 2008), such trend cannot be accounted for by melting or crystallization processes, but is consistent with magma mixing. Similar correlations are also manifest in major element Harker diagrams (Fig. 7), indicating that end-member mixing occurred in certain proportions, so do the linear trends for most trace elements (Fig. 8).

Since experimental works demonstrate that liquid-state isotope diffusion is up to two orders of magnitude more rapid than elemental diffusion (Baker, 1989; Lesher, 1994), isotopic equilibration between silicates of contrasted compositions is generally more easily achieved than chemical equilibration, as is exemplified by the relatively isotopic uniformity in numerous MME-granitoid associations (Barbarin, 2005; Poli and Tommasini, 1999). This eclipses the application of the classical mixing model based on the isotopic compositions of potential end-members to the evaluation of the hybridization extent in the products originating from mafic–felsic interaction.

Alternatively, we conducted two-component calculation based on major elements by following the practice of Janoušek et al. (2004) and Słaby and Martin (2008), to unravel the extent of hybridization in the present diorites and granodiorites. The calculation uses an average mafic end-member and an average felsic end-member magma composition. The results for an average hybrid are given in a $C_{(\text{hybrid diorite-granodiorite})} - C_{(\text{felsic end-member magma})}$ vs. $C_{(\text{mafic end-member})} - C_{(\text{felsic end-member})}$ diagram (Fig. 14; Fourcade and Allégre, 1981), where C represents the concentration of an oxide. In a case of mixing, all of the points on such a diagram would plot on a straight line passing through the origin and with a slope that represents the degree of mixing (Słaby and Martin, 2008). The line ($R^2 = 0.9949$) for the diorites and granodiorites going exactly through the origin, supports the mixing hypothesis and shows that an average hybrid can be explained by the mixing of 68% gabbroic and 32% granitic magma.

Although magma mixing can explain the global trend of the elemental variations, it fails to fully account for the deviation of certain trace elements from the mixing trend in some diagrams. We suggest that such irregular elemental variations and largely homogeneous isotopic signature among various rock types may be attributed to endo-hybridization, a mixing process by hybridization of magmas at different stages of the evolution along the liquid line of descent (Duchesne et al., 1998). As in the case of the post-collisional Tismana pluton from the South Carpathians of Romania (Duchesne et al., 1998), this process, together with subsequent differentiation and minor middle to lower crustal contamination, can explain the varied geochemical characteristics of the intermediate rocks, such as their elevated Zr and Hf abundances and most evolved Sr–Nd compositions in some granodiorite samples. However, the exhaustive evaluation on these processes is beyond the scope of this paper, given the limited space and numerous uncertainties involved in the evaluation.

7.2.4. Intra-mafic suite evolution

For the gabbroic rocks from the YHY stock, their moderate Mg number (40–59), low Cr (5–125 ppm) and Ni (13–31 ppm) concentrations indicate that they do not represent primary magmas, but may have experienced some fractionation crystallization and mineral accumulation, as reflected by typical lithologies of the stock. The former process is also evident on most Harker diagrams (Fig. 7). The decrease in CaO, MgO, Fe_2O_3 and TiO_2 with increasing SiO_2 , are most likely related to fractional crystallization of plagioclase, pyroxene, apatite, magnetite and ilmenite, while the positive correlations of K_2O and Al_2O_3 with SiO_2 indicate that K-feldspar in the residual magma

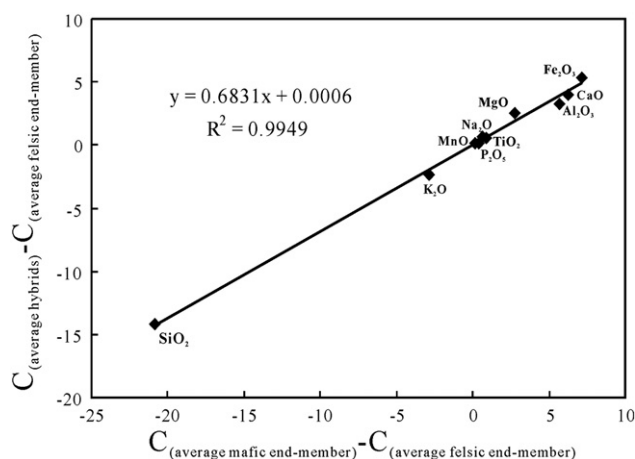


Fig. 14. $C_{(\text{hybrid diorite-granodiorite})} - C_{(\text{felsic end-member magma})}$ vs. $C_{(\text{mafic end-member})} - C_{(\text{felsic end-member})}$ diagram (Fourcade and Allégre, 1981) for the average hybrid diorite-granodiorite.

had increasingly accumulated with the fractional crystallization of other minerals. The leuconorites, with their relatively high Cr contents and typical REE patterns (Fig. 9) for massif-type anorthosite–leuconorite association (e.g., Ashwal, 1993), argue for a cumulate origin. With their similar Sr–Nd isotopic compositions, the gabbroic and leuconoritic rocks could be complementary products from a closed system crystal fractionation process in mafic magma chambers.

The MME, with their silica contents from 49.2 to 54.7%, well corresponds to the general mafic to intermediate (45–55% SiO₂) composition for the MME in granitic systems worldwide (Bonin, 2004). They also have other major element contents and REE patterns similar to those of the gabbroic rocks from the YHY stock. Therefore, they may represent modified blobs of the mafic magma from the same mantle source as the YHY gabbroic rocks. However, the higher Mg-number and Ni contents in MME suggest a less-evolved nature than the gabbroic rocks. The dominance of hornblende and biotite in the MME as the mafic minerals further points to a relatively water-rich magma, because >3 wt.% H₂O is necessary for early crystallization of amphibole from a basaltic melt (Eggler, 1972). Moreover, the MME display comparable whole-rock Sr–Nd and zircon Hf isotopic signatures to those of their host diorites and granodiorites. This is consistent with the commonly accepted petrogenetic scenario for the MME associated with calc-alkaline granitoids (Bonin, 2004) and experimental evidence (Leshner, 1994), indicating intensive isotopic exchange between hot mafic magma and cooler felsic host crystallizing magmas.

The mafic dykes, with their nearly even thickness and occasional angular host granodiorite xenoliths in them (Fig. 2j), clearly show that they represent injection of mafic magma into early fractures in the cooling and crystallizing diorite–granodiorite. The uniform mineral composition and similar chemical affinity in the mafic dyke and MME indicate that they could be co-genetic, whereas the distinct, more primitive isotopic signatures of some dyke samples than MME and their host rocks suggest limited mixing and mingling, which prohibited complete isotopic equilibration. In addition, two mafic dyke samples with extremely low HREE abundances may either come from a deeper source or experience extensive fractionation of phases such as amphibole and pyroxene, as reflected by the Cr–Ni fractionation vector plot (Fig. 15).

All told, the field relations, chronological and geochemical data consistently document a sequence of enriched SCLM-derived mafic magmas, from the earliest homogeneous gabbroic stock through the intermediary MME to the latest mafic dykes with chilled margins, during the crystallization history of the Guyang batholith. Such episodic mafic magma emplacement throughout the crystallization of granite is not only reminiscent of numerous case examples worldwide, like the Sierra Nevada batholith (Barbarin, 2005) and the Hercynian Karkonosze pluton (Słaby and Martin, 2008), but also is consistent with the experimental work of Hallot et al. (1994, 1996). As such, the mafic magma succession in the Guyang batholith signifies a continuous response of mantle-derived mafic magma to the evolved viscosity contrast of the interacting magmas from evolved magma reservoirs. The progenitor mafic magmas from a metasomatized lithospheric mantle formed a magma chamber at the mantle–crust interface possibly due to upwelling of asthenosphere. It is there that they experienced fractional crystallization forming gabbro and gabbroic diorite, with crystal accumulation forming leuconorite. Besides this, they also provide the heat source for melting the extant lower crust and newly accreted lower crust during the previous subduction epoch to yield felsic magmas. The injection of the evolved mafic magma into a similarly low-viscosity, melt-rich granitic mass allowed more complete mixing to produce homogeneously hybridized diorite–granodiorite, while later injections into more fully crystallized hybrid rocks generated spheroidal MME. Lastly, injection into almost totally crystallized magma bodies, where the viscosity contrast is very high, resulted in dykes with sharp contacts and chilled margins.

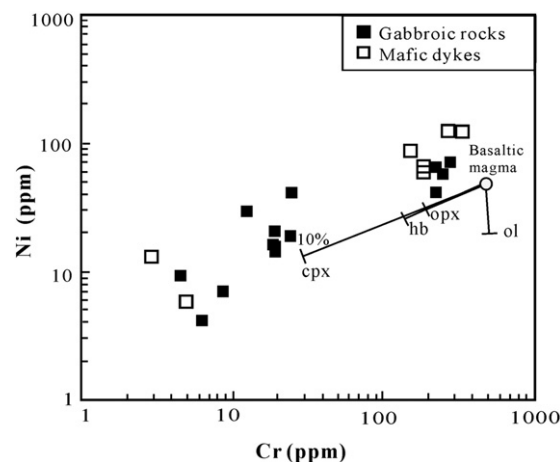


Fig. 15. Ni vs. Cr plots for the mafic rocks from the Guyang batholith. Directions of fractionation vectors for olivine, clinopyroxene, orthopyroxene and hornblende are based on partition coefficients from Rollinson (1993).

7.3. Geodynamic setting

For the Early Permian magmatic rocks along the northern NCC, the current prevailing model is that they have been developed under an active continental arc setting associated with the subduction process in the Solonker suture zone (Zhang et al., 2007, 2009a,b). However, this not only seems to be at odds with the recent proposition that the subduction in the zone has not initiated until ca. 294–280 Ma (Jian et al., 2010), but also contradicts with the reworking-dominated continental crustal evolution in the northern NCC during late Paleozoic. As documented by this study and previous investigations (Zhang et al., 2009a,b,d), the Carboniferous and Early Permian magmatic rocks from the northern NCC consistently displayed Archean to Paleoproterozoic whole-rock Nd and zircon Hf model ages. This implies that only slight amounts of, if any, juvenile materials have been added within the northern NCC during this period. Such reworking-dominated scenario sharply contrasts with the general situation of significant crustal growth for an active margin, like the cases of the Mesozoic to Cenozoic South American Andes (e.g., Faure, 2001; Lucassen et al., 2006), the Mesozoic North American Sierra Nevada (Wenner and Coleman, 2004) and the Late Paleozoic northern block of the north China–Mongolia tract (Chen et al., 2000; Zhang et al., 2008; 2011). Therefore, we propose that the northern NCC was not an active margin during Late Paleozoic time but in the position of a passive margin environment.

Given its dual cratonic and reactivated characters, the Late Paleozoic situation in the northern NCC is reminiscent of a metacratonic evolution (Abdelsalam et al., 2002; Liégeois et al., 2003). As exemplified by the Saharan metacraton, a metacraton evolves from a region between a rigid, unaffected craton and a mobile belt completely affected by an orogeny (Abdelsalam et al., 2002; Liégeois et al., 2003). It has been remobilized during an orogenic event but is still recognizable through its rheological, petrologic, geochronological and isotopic characteristics (De Waele et al., 2006; Fezaa et al., 2010; Liégeois et al., 2003). Typical expressions include episodic magmatism with long-term memory of cratonic geochemical signature, largely undisturbed deposition, suturing with neighboring juvenile terranes, recurrently activated mega-shear zones, co-existing low- and high-grade metamorphism, and favorable fluid circulation (Abdelsalam et al., 2002; De Waele et al., 2006; Ennih and Liégeois, 2008; Liégeois et al., 2003). In general, a metacratonic evolution can be driven by a succession of events including collisional process, linear lithospheric delamination along mega-shear zones, regional extension and post-collisional dismembering (Abdelsalam et al., 2002; Liégeois et al., 2003). These processes are prone to facilitate hot asthenospheric upwelling and to promote melting in various sources including the ascended asthenosphere, the enriched lithosphere and the overlying lower crust.

This is just the case in the northern NCC during the Late Paleozoic. First, the Archean–Paleoproterozoic basement rocks and the Carboniferous plutonic rocks commonly bear the Variscan greenschist facies thermal metamorphic or deformational overprints (Hu et al., 2003; Nie et al., 2002; Zhang et al., 1999; Zhang et al., 2007, 2009a,d), while the high-grade metamorphism is recorded by the Carboniferous retrograded eclogites (Ni et al., 2006). With these eclogites as the indicator of possible extinct oceanic lithosphere (Ni et al., 2006), it is inferred that the Chifeng–Bayan Obo fault represents a feasible suture between the northern NCC and the Early–Mid Paleozoic southern orogen of north China (Jian et al., 2010). Second, a continuous deposition of passive margin style is recorded by the Upper Carboniferous to Permian coal-bearing strata along the northern NCC, with only a few negligible pyroclastic sequences of cratonic origin (Cope et al., 2005; Yang et al., 2006). Third, favorable fluid circulation contributes much to the spectacular coeval gold mineralization in this region (Lu et al., 2009; Nie et al., 2002; Zhang et al., 1999).

Last but not the most revealing metacratonic expression comes from concurrent magmatism. As the preceding enumeration depicts, the Early Permian igneous rocks from the northern NCC and the neighboring orogenic belt constitute a magmatic province with coverage of more than 200,000 km² across the northern China–Mongolia tract (Zhang and Zhai, 2010). It exhibits temporal and spatial distribution, rock constituent, magma genesis and metamorphic style typical of post-collisional magmatism. Being a critical phase between collisional and post-orogenic stages, post-collisional setting generally defines a complex period that can include geological episodes such as large movements along transcurrent shear zones, lithosphere delamination, subduction of small oceanic plates and rifting (e.g., Bonin, 2004; Liégeois, 1998). As demonstrated in the world-wide orogenic belts of various ages, post-collisional magmatism is distinctive with widespread spatial distribution, a wide variety of magmas including predominant high-K calc-alkaline series and sporadic peraluminous and alkaline-peralkaline series, free from collision-related metamorphism and common linkage to horizontal movements along major shear zones (Bonin, 2004). Case examples include the Neoproterozoic to Cambrian (580–479 Ma) high-K calc-alkaline mafic–felsic associations from the East African orogen (Küster and Harms, 1998), the Carboniferous to Early Permian granitoid suites in the European Variscides (Altherr et al., 2000; Bonin, 2004; Janoušek et al., 2004; Poli and Tommasini, 1991, 1999; Slaby and Martin, 2008; Topuz et al., 2010), and the Late Carboniferous to Permian (ca. 320–270 Ma) granitoids in the North Xinjiang of the CAO (Han et al., 2010).

The magmatic province herein is not confined to any specific belts but extends across major suturing zones. Its distribution at specific regions is closely related with large horizontal movements along major deep-seated faults (e.g., Nie et al., 2002; Zhang et al., 2009a,b; this study). In regard to rock types, it features predominant medium- to high-K calc-alkaline I-type granitoids, volumetrically minor but widely distributed components of A-type granite, peraluminous S-type granite and mafic–ultramafic complexes. Specifically, the diffuse distribution of such extension-sensitive components as the A-type granites and their extrusive equivalents (Blight et al., 2010b; Kovalenko et al., 2006; Luo et al., 2009; Shi et al., 2004; Wu et al., 2002; Yarmolyuk et al., 2008; Zhang et al., 2008) across all terranes argues for a prevailing extensional regime (Zhang and Zhai, 2010). This cannot be readily attributed to ridge subduction, although the mechanism may account for the increased heat necessary to cause partial melting of the crust (Jian et al., 2010), because it requires that ridge subduction must have occurred nearly simultaneously in all the terranes. Instead, basaltic underplating due to post-collisional lithospheric delamination may present an alternative mechanism for their generation, as in the case of the northern Xinjiang of the CAO (Han et al., 2010).

With the affiliation of the Early Permian magmatic rocks from the northern NCC to a metacratonic post-collisional transtensional regime, we alternatively suggest that the short life cycle (<30 Ma) of the

Solonker ophiolitic rocks as defined by Jian et al. (2010) may be compatible with the time scale of restricted oceanic plates that could exist during a post-collisional stage.

8. Conclusion: A pluton construction model

The multiple-step deep-seated crust–mantle interaction processes, propelled by sustained heat engine due to linear lithospheric delamination and hot asthenospheric upwelling along mega-shear zones, led to the construction of the Guyang batholith within a metacratonic passive margin, as detailed in the following:

(1) Mafic magmas from a metasomatized lithospheric mantle are emplaced at the mantle–crust interface, a mechanical boundary between a ductile lower crust and a less ductile upper mantle. They tend to be trapped here due to their higher density to form mafic magma chambers below the thick continental lid. Subsequent high-pressure fractionation of olivine and pyroxene yielded basaltic melts parental to the YHY gabbro–leuconorite suite, with cumulate material forming newly accreted lower crust. (2) Mixtures of the underplated lower crust and old Precambrian crustal component are partially re-melted by heat from further underplating and rising asthenosphere during continued extension. (3) The resultant melts may combine with evolved mafic melts to form pools of thoroughly mixed intermediate to felsic magma at depth and these pools coalesce to produce homogeneous hybrid magmas that move into the middle crust and differentiate to form diorite and granodiorite. (4) During ascent and emplacement of hybrid magmas, mafic melts replenished from magma pools were injected into the open system of granitoid magma differentiation and were disrupted into small scattered blobs in the moving granitoid magma. Mingling and local mixing at the emplacement level produced various types of MME. (5) During the latest phase and when the felsic magma is largely crystallized, the mafic magma is channeled into the early fractures of an essentially solid granitoid rock to produce undisturbed mafic dykes.

Supplementary materials related to this article can be found online at doi: [10.1016/j.lithos.2011.03.008](https://doi.org/10.1016/j.lithos.2011.03.008).

Acknowledgements

We would like to thank Yu-Guang Ma for his help with zircon CL imaging; He Li and Xin-Di Jin for their help in major- and trace-element analysis; Chao-Feng Li for help in Sr–Nd isotope analyses; Q.L. L and Y. Liu for arrangement and technical help in SIMS analyses. We are also grateful to Profs. J. P. Liégeois, Nelson Eby and an anonymous reviewer for their constructive comments. Special thanks go to Ms. Hui Ren for her encouragement during this laborious writing. This study is financially supported by the Knowledge Innovation Program of the Chinese Academy of Sciences (Grant nos. KZCX2-YW-QN115 and KZCX2-YW-Q4-04) and the National Natural Science Foundation of China (Grant nos. 90914008 and 40873026).

References

- Abdelsalam, M., Liégeois, J.P., Stern, R.J., 2002. The Saharan metacraton. *Journal of African Earth Science* 34, 119–136.
- Altherr, R., Holl, A., Hegner, E., Langer, C., Kreuzer, H., 2000. High-potassium, calcalkaline I-type plutonism in the European Variscides: northern Vosges (France) and northern Schwarzwald (Germany). *Lithos* 50, 51–73.
- Anderson, T., 2002. Corrections of common lead in U–Pb analyses that do not report ²⁰⁴Pb. *Chemical Geology* 192, 59–79.
- Anderson, J.L., Smith, D.R., 1995. The effects of temperature and fO₂ on the Al-in-hornblende barometer. *American Mineralogist* 80, 549–559.
- Anderson, J.L., Barth, A., Wooden, J., Mazdab, F., 2008. Thermometers and thermobarometers in granitic systems. *Reviews in Mineralogy and Geochemistry* 69, 121–142.
- Ashwal, L.D., 1993. *Anorthositic, Minerals and Rocks*, Vol. 21. Springer-Verlag, Berlin, pp. 1–422.
- Atherton, M.P., Petford, N., 1993. Generation of sodium-rich magmas from newly underplated basaltic crust. *Nature* 362, 144–146.
- Badarch, G., Cunningham, W.D., Windley, B.F., 2002. A new terrane subdivision for Mongolia: implications for the Phanerozoic crustal growth of Central Asia. *Journal of Asian Earth Sciences* 21, 87–104.

- Baker, D.R., 1989. Tracer versus trace element diffusion: diffusional decoupling of Sr concentration from Sr isotope composition. *Geochimica et Cosmochimica Acta* 53, 3015–3023.
- Bao, Q.Z., Zhang, C.J., Wu, Z.L., 2007. SHRIMP U–Pb zircon geochronology and its implications of Carboniferous period quartz diorite in Baiyingaole area, Inner Mongolia. *Journal of Jilin University (Earth Science edition)* 37, 15–23.
- Barbarin, B., 1991. Enclaves of the Mesozoic calc-alkaline granitoids of the Sierra Nevada batholith, California. In: Didier, J., Barbarin, B. (Eds.), *Enclaves and Granite Petrology. : Developments in Petrology*, 13. Elsevier, Amsterdam, pp. 135–153.
- Barbarin, B., 1999. A review of the relationships between granitoid types, origins and their geodynamic environments. *Lithos* 46, 605–626.
- Barbarin, B., 2005. Mafic magmatic enclaves and mafic rocks associated with some granitoids of the central Sierra Nevada batholith, California: nature, origin, and relations with the hosts. *Lithos* 80, 155–177.
- Blight, J.H.S., Crowley, Q.G., Petterson, M.G., Cunningham, D., 2010a. Granites of the southern Mongolia Carboniferous arc: new geochronological and geochemical constraints. *Lithos* 116, 35–52.
- Blight, J.H.S., Petterson, M.G., Crowley, Q.G., Cunningham, D., 2010b. The Oyut Ulaan volcanic group: stratigraphy, magmatic evolution and timing of Carboniferous arc development in SE Mongolia. *Journal of the Geological Society of London* 167, 491–509.
- Bonin, B., 2004. Do coeval mafic and felsic magmas in post-collisional to within-plate regimes necessarily imply two contrasting, mantle and crustal, sources? A review. *Lithos* 78, 1–24.
- Castillo, P.R., Janney, P.E., Solidum, R.U., 1999. Petrology and geochemistry of Camiguin Island, southern Philippines: insights to the source of adakites and other lavas in a complex arc setting. *Contributions to Mineralogy and Petrology* 134, 33–51.
- Chen, B., Jahn, B.M., Wilde, S.A., Xu, B., 2000. Two contrasting Paleozoic magmatic belts in northern Inner Mongolia, China: petrogenesis and tectonic implications. *Tectonophysics* 328, 157–182.
- Chen, B., Jahn, B.M., Tian, W., 2009a. Evolution of the Solonker suture zone: constraints from zircon U–Pb ages, Hf isotopic ratios and whole-rock Nd–Sr isotope compositions of subduction and collision-related magmas and forearc sediments. *Journal of Asian Earth Sciences* 34, 245–257.
- Chen, B., Suzuki, K., Tian, W., Jahn, B.M., Ireland, T., 2009b. Geochemistry and Os–Nd–Sr isotopes of the Gaositai Alaskan-type ultramafic complex from the northern North China craton: implications for mantle–crust interaction. *Contributions to Mineralogy and Petrology* 158, 683–702.
- Clemens, J.D., Darbyshire, D.P.F., Flinders, J., 2009. Sources of post-orogenic calcalkaline magmas: the Arrochar and Garaball Hill–Glen Fyne complexes, Scotland. *Lithos* 112, 524–542.
- Cope, T., Ritts, B.D., Darby, B.J., Fildani, A., Graham, S.A., 2005. Late Paleozoic sedimentation on the northern margin of the North China Block: implications for regional tectonics and climate change. *International Geology Review* 47, 270–296.
- Davis, G.A., Wang, C., Zheng, Y., Zhang, J., Zhang, C., Gehrels, G.E., 1998. The enigmatic Yinshan fold and thrust belt of northern China: new views on its intraplate contractional styles. *Geology* 26, 43–46.
- de Jong, K., Xiao, W., Windley, B.F., Masago, H., Lo, C.H., 2006. Ordovician ⁴⁰Ar–³⁹Ar phengite ages from the blueschist-facies Ondor Sum subduction-accretion complex (Inner Mongolia) and implications for the early Paleozoic history of continental blocks in China and adjacent areas. *American Journal of Sciences* 306, 799–845.
- De Waele, B., Liégeois, J.P., Nemchin, A.A., Tembo, F., 2006. Isotopic and geochemical evidence of proterozoic episodic crustal reworking within the irumide belt of south-central Africa, the southern metacratonic boundary of an Archaean Bangweulu craton. *Precambrian Research* 148, 225–256.
- Defant, M.J., Drummond, M.S., 1990. Derivation of some modern arc magmas by melting of young subducted lithosphere. *Nature* 347, 662–665.
- Duchesne, J.C., Berza, T., Liégeois, J.P., Auwera, J.V., 1998. Shonohitic liquid line of descent from diorite to granite: the Late Precambrian post-collisional Tismana pluton (south Carpathians, Romania). *Lithos* 45, 281–303.
- Eggler, D.H., 1972. Amphibole stability in H₂O-undersaturated calc-alkaline melts. *Earth and Planetary Science Letters* 15, 28–34.
- Ennih, N., Liégeois, J.P., 2008. The boundaries of the West African craton, with special reference to the basement of the Moroccan metacratonic anti-Atlas belt. *Geological Society, London, Special publications*, 297, pp. 1–17.
- Fan, H.R., Hu, F.F., Yang, K.F., Wang, K.Y., Liu, Y.S., 2009. Geochronology framework of late Paleozoic dioritic–granitic plutons in the Bayan Obo area, Inner Mongolia, and tectonic significance. *Acta Petrologica Sinica* 25, 2933–2938.
- Faure, G., 2001. *Origin of Igneous Rocks: The Isotopic Evidence*. Springer-Verlag, Berlin.
- Fezaa, N., Liégeois, J.P., Abdallah, N., Cherfouh, E.H., Waele, B.D., Bruguier, O., Ouabadi, A., 2010. Late Ediacaran geological evolution (573–555 Ma) of the Djanet terrane, Eastern Hoggar, Algeria, evidence for a Murzukian intracontinental episode. *Precambrian Research* 180, 299–327.
- Flèche, La, Camiré, E.G., Jenner, G.A., 1998. Geochemistry of post-Acadian, Carboniferous continental intraplate basalts from the Maritimes Basins, Magdalen Islands, Québec, Canada. *Chemical Geology* 148, 115–136.
- Fourcade, S., Allègre, C.J., 1981. Trace element behavior in granite genesis: a case study. The calc-alkaline plutonic association from Querigut complex (Pyrénées, France). *Contributions to Mineralogy and Petrology* 76, 177–195.
- Frost, B.R., Barnes, C.G., Collins, W.J., Arculus, R.J., Ellis, D.J., Frost, C.D., 2001. A geochemical classification for granitic rocks. *Journal of Petrology* 42, 2033–2048.
- Gao, S., Rudnick, R.L., Yuan, H.L., Liu, X.M., Liu, Y.S., Xu, W.L., Ayers, J., Wang, X.C., Wang, Q.H., 2004. Recycling lower continental crust in the North China Craton. *Nature* 432, 892–897.
- Griffin, W.L., Wang, X., Jackson, S.E., Pearson, N.J., O'Reilly, S.Y., Xu, X.S., Zhou, X.M., 2002. Zircon chemistry and magma mixing: SE China: in situ analysis of Hf isotopes, Tonglu and Pingtan igneous complexes. *Lithos* 61, 237–269.
- Griffin, W.L., Powell, W.J., Pearson, N.J., O'Reilly, S.Y., 2008. GLITTER: data reduction software for laser ablation ICP–MS. In: Sylvester, P. (Ed.), *Laser Ablation–ICP–MS in the Earth Sciences: Mineralogical Association of Canada Short Course Series, Volume 40*, pp. 204–207. Appendix 2.
- Hallot, E., Auvray, B., de Bremond d'Ars, J., Davy, P., Martin, H., 1994. New injection experiments in non-Newtonian fluids. *Terra Nova* 6, 274–281.
- Hallot, E., Davy, P., de Bremond d'Ars, J., Auvray, B., Martin, H., van Damme, H., 1996. Non-Newtonian effects during injection in partially crystallised magmas. *Journal of Volcanology and Geothermal Research* 71, 31–44.
- Han, B.F., Guo, Z.J., Zhang, Z.C., Zhang, L., Chen, J.F., Song, B., 2010. Age, geochemistry, and tectonic implications of a late Paleozoic stitching pluton in the North Tian Shan suture zone, western China. *Geological Society of America Bulletin* 122, 627–640.
- He, H.Y., Wang, X.L., Zhou, Z.H., Wang, F., Boven, A., Shi, G.H., Zhu, R.X., 2004. Timing of the Jiufotang Formation (Jehol Group) in Liaoning, northeastern China, and its implications. *Geophysical Research Letters* 31, L12605. doi:10.1029/2004GL019790.
- Hibbard, M.J., 1991. Textural anatomy of twelve magma-mixed granitoid systems. In: Didier, J., Barbarin, B. (Eds.), *Enclaves and Granite Petrology. : Developments in Petrology*, 13. Elsevier, Amsterdam, pp. 431–444.
- Holland, T., Blundy, J., 1994. Non-ideal interactions in calcic amphiboles and their bearing on amphibole–plagioclase thermometry. *Contributions to Mineralogy and Petrology* 116, 433–447.
- Hong, D.W., Wang, T., Tong, Y., 2007. An outline about granitoids in China. *Geological Reviews* 52, 9–16 (Supp.) (In Chinese with English abstracts).
- Hu, L., Song, H.L., Yan, D.P., Hu, D.G., 2003. The ⁴⁰Ar/³⁹Ar geochronology constraint and geological significance of mylonites in Shangyi–Chicheng fault belt on the north of North China Craton. *Science in China (D)* 46, 1134–1142.
- Inner Mongolian Bureau of Geology and Mineral Resources (IMBGMR). 1972. 1:200,000 scale geological map of Guyang and notes.
- Jahn, B.M., 2004. The Central Asian Orogenic Belt and growth of the continental crust in the Phanerozoic. In: Malpas, J., Fletcher, C.J.N., Ali, J.R., Aitchison, J.C. (Eds.), *Aspects of the Tectonic evolution of China*. Geological Society, London, Special Publications, 226, pp. 73–100.
- Jahn, B.M., Auvray, B., Cornichet, J., Bai, Y.L., Shen, Q.H., Liu, D.Y., 1987. 3.5 Ga old amphibolites from eastern Hebei province, China: field occurrence, petrology, Sm–Nd isochron age and REE geochemistry. *Precambrian Research* 34, 311–346.
- Janoušek, V., Braithwaite, C.J.R., Bowes, D.R., Gerdes, A., 2004. Magma-mixing in the genesis of Hercynian calc-alkaline granitoids: an integrated petrographic and geochemical study of the Sázava intrusion, Central Bohemian Pluton, Czech Republic. *Lithos* 78, 67–99.
- Jian, P., Liu, D.Y., Kroner, A., Windley, B.F., Shi, Y.R., Zhang, F.Q., Shi, G.H., Miao, L.C., Zhang, W., Zhang, Q., Zhang, L., Ren, J., 2008. Time scale of an Early to Mid-Paleozoic orogenic cycle of the long-lived Central Asian Orogenic belt, Inner Mongolia of China: implications for continental growth. *Lithos* 101, 233–259.
- Jian, P., Liu, D.Y., Kroner, A., Windley, B.F., Shi, Y.R., Zhang, W., Zhang, F.Q., Miao, L.C., Zhang, L., Tomurhuu, D., 2010. Evolution of a Permian intraoceanic arc–trench system in the Solonker suture zone, Central Asian orogenic belt, China and Mongolia. *Lithos* 118, 169–190.
- Jiang, N., Liu, Y.S., Zhou, W.G., Yang, J.H., Zhang, S.Q., 2007. Derivation of Mesozoic adakitic magmas from ancient lower crust in the North China Craton. *Geochimica et Cosmochimica Acta* 71, 2591–2608.
- Killian, R., Stern, C.R., 2002. Constraints on the interaction between slab melts and the mantle wedge from adakitic glass in peridotite xenoliths. *European Journal of Mineralogy* 14, 25–36.
- Koppers, A.A.P., 2002. ArArCALC-software for ⁴⁰Ar/³⁹Ar age calculations. *Computers and Geosciences* 28, 605–619.
- Kovalenko, V.I., Yarmoluyk, V.V., Sal'nikova, E.B., Kozlovsky, A.M., Kotov, A.B., Kovach, V.P., Savatenkov, V.M., Vladvkin, N.V., Ponomarchuk, V.A., 2006. Geology, geochronology and geodynamics of the Khan Bogd alkali granite pluton in southern Mongolia. *Geotectonics* 40, 450–466.
- Kusky, T.M., Windley, B.F., Zhai, M.G., 2007. Tectonic evolution of the North China Block: from orogen to craton to orogen. In: Zhai, M.G., Windley, B.F., Kusky, T.M., Meng, Q.R. (Eds.), *Mesozoic sub-continental lithospheric thinning under eastern Asia: Geological Society, London, Special Publication*, 280, pp. 1–34.
- Küster, D., Harms, U., 1998. Post-collisional potassic granitoids from the southern and northwestern parts of the Late Neoproterozoic East African Orogen: a review. *Lithos* 45, 177–195.
- Lamb, M.A., Badarch, G., 2001. Paleozoic sedimentary basins and volcanic arc systems of southern Mongolia; new geochemical and petrographic constraints. In: Hendrix, M.S., Davis, G.A. (Eds.), *Paleozoic and Mesozoic Tectonic Evolution of Central and Eastern Asia: From Continental Assembly to Intracontinental Deformation*. Memoirs, 194. Geological Society of America, pp. 117–149.
- Landenberger, B., Collins, W.J., 1996. Derivation of A-type granites from a dehydrated charnockitic lower crust: evidence from the Chaelundi complex, Eastern Australia. *Journal of Petrology* 37, 145–170.
- Le Maitre, R.W., 2002. *Igneous Rocks: A Classification and Glossary of Terms*, 2nd edn. Cambridge University Press, Cambridge. 236 pp.
- Leake, B.E., Woolley, A.R., Arps, C.E.S., Birch, W.D., Gilbert, M.C., Grice, J.D., Hawthorne, F.C., Kato, A., Kisch, H.J., Krivovichev, V.G., Linthout, K., Laird, J., Mandarin, J.A., Maresch, W.V., Nickel, E.H., Rock, N.M.S., Schumacher, J.C., Smith, D.C., Stephenson, N.C.N., Ungaretti, L., Whittaker, E.J.W., Youzhi, G., 1997. Nomenclature of amphiboles: report of the subcommittee on amphiboles of the International Mineralogical Association, Commission on New Minerals and Mineral Names. *American Mineralogist* 82, 1019–1037.
- Leshner, C.E., 1994. Kinetics of Sr and Nd exchange in silicate liquids: theory, experiments, and applications to uphill diffusion, isotopic equilibration, and irreversible mixing of magmas. *Journal of Geophysical Research* B5 (99), 9585–9604.

- Li, Q.L., Chen, F.K., Guo, J.H., Li, X.H., Yang, Y.H., Siebel, W., 2007. Zircon ages and Nd–Hf isotopic composition of the Zhaertaogou Group (Inner Mongolia): evidence for Early Proterozoic evolution of the northern North China Craton. *Journal of Asian Earth Sciences* 30, 573–590.
- Li, X.H., Liu, Y., Li, Q.L., Guo, C.H., Chamberlain, K.R., 2009. Precise determination of Phanerozoic zircon Pb/Pb age by multi-collector SIMS without external standardization. *Geochemistry Geophysical Geosystem* 10, Q04010. doi:10.1029/2009GC002400.
- Liégeois, J.P., 1998. Preface – some words on the post-collisional magmatism. *Lithos* 45, XV–XVII.
- Liégeois, J.P., Navez, J., Hertogen, J., Black, R., 1998. Contrasting origins of post-collisional high-calc-alkaline-shononitic and alkaline-peralkaline granitoids. The use of sliding normalization. *Lithos* 45, 1–28.
- Liégeois, J.P., Latouche, L., Boughrara, M., Navez, J., Guiraud, M., 2003. The LATEA metacraton (central Hoggar, Tuareg shield, Algeria): behaviour of an old passive margin during the Pan-African orogeny. *Journal of African Earth Sciences* 37, 161–190.
- Liu, Y.S., Gao, S., Yuan, H.L., Zhou, L., Liu, X.M., Wang, X.C., Hu, Z.C., Wang, L.S., 2004. U–Pb zircon ages and Nd, Sr, and Pb isotopes of lower crustal xenoliths from North China Craton: insights on evolution of lower continental crust. *Chemical Geology* 211, 87–109.
- Liu, J.F., Chi, X.G., Zhang, X.Z., Ma, Z.H., Zhao, Z., Wang, T.F., Hu, Z.C., Zhao, X.Y., 2009. Geochemical characteristics of Carboniferous quartz-diorite in the southern Xiwuqi area, Inner Mongolia and its tectonic significance. *Acta Geologica Sinica* 83, 365–376.
- Liu, Y., Gao, S., Hu, Z., Gao, C., Zong, K., Wang, D., 2010. Continental and oceanic crust recycling-induced melt peridotite interactions in the Trans-North China orogen: U–Pb dating, Hf isotopes and trace elements in zircons of mantle xenoliths. *Journal of Petrology* 51, 537–571.
- López, S., Castro, A., 2001. Determination of the fluid-absent solidus and supersolidus phase relationships of MORB-derived amphibolites in the range 4–14 kbar. *American Mineralogist* 86, 1396–1403.
- Lu, Y.H., Li, W.B., Lai, Y., 2009. Time and tectonic setting of hosting porphyry of the Hadamiao gold deposit in Xianghuangqi, Inner Mongolia. *Acta Petrologica Sinica* 25, 2615–2620.
- Lucassen, F., Kramer, W., Bartsch, V., Wilke, H.G., Franz, G., Romer, R.L., Dulski, P., 2006. Nd, Pb, and Sr isotope composition of juvenile magmatism in the Mesozoic large magmatic province of northern Chile (18–27°S): indications for a uniform subarc mantle. *Contributions to Mineralogy and Petrology* 152, 571–589.
- Ludwig, K., 2001. User manual for isoplot/EX (2.49). Berkeley Geochronology Center Special Publication No. 1a. . 55 pp.
- Lugmair, G.W., Marti, K., 1978. Lunar initial ¹⁴³Nd/¹⁴⁴Nd: differential evolution of the lunar crust and mantle. *Earth and Planetary Science Letters* 39, 349–357.
- Luo, H.L., Wu, T.R., Li, Y., 2007. Geochemistry and SHRIMP dating of the Kebu massif from Wulatezhongqi, Inner Mongolia: evidence for the Early Permian underplating beneath the North China Craton. *Acta Petrologica Sinica* 23, 755–766.
- Luo, H.L., Wu, T.R., Zhao, L., 2009. Zircon SHRIMP U–Pb dating of Wuliangtsai A-type granite on the northern margin of the North China plate and tectonic significance. *Acta Petrologica Sinica* 25, 515–526.
- Macpherson, C.G., Dreher, S., Matthew, T., Thirlwall, F., 2006. Adakites without slab melting: High pressure differentiation of island arc magma, Mindanao, the Philippines. *Earth and Planetary Science Letters* 243, 581–593.
- McCulloch, M.T., Gamble, J.A., 1991. Geochemical and geodynamical constraints on subduction zone magmatism. *Earth and Planetary Science Letters* 102, 358–374.
- McMillan, A., Harris, N.B.W., Holness, M., Ashwal, L., Kelley, S., Rambelosen, R., 2003. A granite–gabbro complex from Madagascar: constraints on melting of the lower crust. *Contributions to Mineralogy and Petrology* 145, 585–599.
- Meng, Q., Zhang, G., 2000. Geological framework and tectonic evolution of Qinling orogen, central China. *Tectonophysics* 323, 183–196.
- Menzies, M.A., 1987. Metasomatic and enrichment processes in lithospheric peridotites, an effect of asthenosphere–lithosphere interaction. In: Menzies, M.A., Hawkesworth, C.J. (Eds.), *Mantle Metasomatism*. Academic Press, London, pp. 313–361.
- Moyen, J.F., 2009. High Sr/Y and La/Yb ratios: the meaning of the 'adakitic signature'. *Lithos* 112, 556–574.
- Ni, Z.Y., Zhai, M.G., Wang, R.M., Tong, Y., 2006. Late Paleozoic retrograded eclogites from within the northern margin of the North China Craton: evidence for subduction of the Paleo-Asian Ocean. *Gondwana Research* 9, 209–224.
- Nie, F.J., Jiang, S.H., Su, X.X., Wang, X.L., 2002. Geological features and origin of gold deposits occurring in the Baotou–Bayan Obo district, south-central Inner Mongolia, People's Republic of China. *Ore Geology Reviews* 20, 139–169.
- Pearce, J.A., Kempton, P.D., Nowell, G.M., Noble, S.R., 1999. Hf–Nd element and isotope perspective on the nature and provenance of mantle and subduction components in western Pacific arc–basin systems. *Journal of Petrology* 11, 1579–1611.
- Peng, P., Guo, J.-H., Zhai, M.-G., Bleeker, W., 2010. Paleoproterozoic gabbro-noritic and granitic magmatism in the northern margin of the North China Craton: evidence of crust–mantle interaction. *Precambrian Research* 183, 635–659.
- Plank, T., Langmuir, C.H., 1993. Tracing trace elements from sediment input to volcanic output at subduction zones. *Nature* 362, 739–742.
- Poli, G.E., Tommasini, S., 1991. Model for the origin and significance of microgranular enclaves in calc-alkaline granitoids. *Journal of Petrology* 32, 657–666.
- Poli, G.E., Tommasini, S., 1999. Geochemical modeling of acid–basic magma interaction in the Sardinia–Corsica batholith: the case study of Sarrabus, southeastern Sardinia, Italy. *Lithos* 46, 553–571.
- Rapp, R.P., Watson, E.B., 1995. Dehydration melting of metabasalt at 8–32 kbar: implications for continental growth and crust–mantle recycling. *Journal of Petrology* 36, 891–931.
- Rapp, R.P., Shimizu, N., Norman, M.D., Applegate, G.S., 1999. Reaction between slab-derived melts and peridotite in the mantle wedge: experimental constraints at 3.8 GPa. *Chemical Geology* 160, 335–356.
- Rapp, R.P., Xiao, L., Shimizu, N., 2002. Experimental constraints on the origin of potassium-rich adakites in eastern China. *Acta Petrologica Sinica* 18, 293–311.
- Rapp, R.P., Shimizu, N., Norman, M.D., 2003. Growth of early continental crust by partial melting of eclogite. *Nature* 425, 605–609.
- Renna, M.R., Tribuzio, R., Tiepolo, M., 2006. Interaction between basic and acid magmas during the latest stages of the post-collisional Variscan evolution: clues from the gabbro–granite association of Ota (Corsica–Sardinia batholith). *Lithos* 90, 92–110.
- Roberts, M.P., Pin, C., Clemens, J.D., Paquette, J.L., 2000. Petrogenesis of mafic and felsic plutonic rock associations: the calcalkaline Quérigut complex, French Pyrenees. *Journal of Petrology* 41, 809–844.
- Rollinson, H.R., 1993. *Using Geochemical Data: Evaluation, Presentation, Interpretation*. London Singapore, Singapore.
- Rudnick, R.L., Gao, S., 2003. Composition of the continental crust. In: Rudnick, R.L. (Ed.), *The Crust, Treatise in Geochemistry*, vol. 3, pp. 1–64.
- Sengör, A.M.C., Natal'in, B.A., Burtman, V.S., 1993. Evolution of the Altai tectonic collage and Palaeozoic crustal growth in Eurasia. *Nature* 364, 299–307.
- Shi, G.H., Miao, L.C., Zhang, F.Q., Jian, P., Fan, W.M., Liu, D.Y., 2004. The age and its regional tectonic implications of the Xilinhaote A-type granites, Inner Mongolia. *Chinese Science Bulletin* 49, 384–389.
- Sisson, T.W., Ratajsti, K., Hankins, W.B., Glazner, A.F., 2005. Voluminous granitic magmas from common basaltic sources. *Contributions to Mineralogy and Petrology* 148, 635–661.
- Słaby, E., Martin, H., 2008. Mafic and felsic magma interaction in granites: the Hercynian Karkonosze Pluton (Sudetes, Bohemian Massif). *Journal of Petrology* 49, 353–391.
- Stacey, J.S., Kramers, J.D., 1975. Approximation of terrestrial lead isotope evolution by a two-stage model. *Earth and Planetary Science Letters* 26, 207–226.
- Steiger, R.H., Jäger, E., 1977. Subcommission on geochronology; convention on the use of decay constants in geochronology and cosmochronology. *Earth and Planetary Science Letters* 36, 359–362.
- Stein, M., Navon, O., Kessel, R., 1997. Chromatographic metasomatism of the Arabian–Nubian lithosphere. *Earth and Planetary Science Letters* 152, 75–91.
- Stern, R.J., 2002. Subduction zones. *Reviews of Geophysics* 40, 1–38.
- Sun, S.S., McDonough, W.F., 1989. Chemical and isotopic systematics of oceanic basalts: implications for mantle composition and processes. In: Saunders, A.D., Norry, M.J. (Eds.), *Magmatism in the Ocean Basins: Geological Society, London, Special Publications*, 42, pp. 528–548.
- Taylor, W.R., 1998. An experimental test of some geothermometer and geobarometer formulations for upper mantle peridotites with application to the thermobarometry of fertile lherzolites and garnet websterite. *Neues Jahrbuch für Mineralogie Abhandlungen* 172, 381–408.
- Topuz, G., Altherr, R., Siebel, W., Schwarz, W.H., Zack, T., Hasözbeek, A., Barth, A.M., Satir, M., Şen, C., 2010. Carboniferous high-potassium I-type granitoid magmatism in the eastern Pontides: the Gümüşhane pluton (NE Turkey). *Lithos* 116, 92–110.
- Vernon, R.H., 1984. Microgranitoid enclaves in granites – globules of hybrid magmas in a plutonic environment. *Nature* 309, 438–439.
- Vernon, R.H., 1991. Interpretation of microstructures of microgranitoid enclaves. In: Didier, J., Barbarin, B. (Eds.), *Enclaves and Granite Petrology: Developments in Petrology*, vol. 13. Elsevier, Amsterdam, pp. 277–291.
- Vyhnal, C.R., Mcswen, J.H.Y., Speer, J.A., 1991. Hornblende chemistry in southern Appalachian granitoids: implications for aluminium hornblende thermobarometry and magmatic epidote stability. *American Mineralogist* 76, 176–188.
- Wang, K.L., Chung, S.L., O'Reilly, S.Y., Sun, S.S., Shinjo, R., Chen, C.H., 2004. Geochemical constraints for the genesis of post-collisional magmatism and geodynamic evolution of the Northern Taiwan Region. *Journal of Petrology* 45, 975–1011.
- Wang, X.L., Zhang, C., Liu, S.W., 2007a. Electron microprobe dating of monazite in granite from Kangbao area, Hebei province. *Acta Petrologica Sinica* 23, 817–822.
- Wang, Q., Wyman, D.A., Xu, J.F., Jian, P., Zhao, Z., Li, C., Xu, W., Ma, J., He, B., 2007b. Early Cretaceous adakitic granites in the Northern Dabie complex, central China: implications for partial melting and delamination of thickened lower crust. *Geochimica et Cosmochimica Acta* 71, 2609–2636.
- Wells, R.A., 1977. Pyroxene thermometry in simple and complex systems. *Contributions to Mineralogy and Petrology* 62, 129–139.
- Wenner, J.M., Coleman, D.S., 2004. Magma mixing and Cretaceous crustal growth: geology and geochemistry of granites in the Central Sierra Nevada batholith, California. *International Geology Review* 46, 880–903.
- Whalen, J.B., Mcnicoll, V.J., Van Staal, C.R., 2006. Spatial, temporal and geochemical characteristics of Silurian collision-zone magmatism, Newfoundland Appalachians: an example of a rapidly evolving magmatic system related to slab breakoff. *Lithos* 89, 377–404.
- Wiedenbeck, M., Alle, P., Corfu, F., Griffin, W.L., Meier, M., Oberli, F., Vonquadt, A., Roddick, J.C., Speigel, W., 1995. Three natural zircon standards for U–Th–Pb, Lu–Hf, trace-element and REE analyses. *Geostandard Newsletter* 19, 1–23.
- Windley, B.F., Alexeev, D., Xiao, W.J., Kroner, A., Badarch, G., 2007. Tectonic models for accretion of the Central Asian Orogenic belt. *Journal of the Geological Society of London* 164, 31–47.
- Woodhead, J.D., Hergt, J.M., Davidson, J.P., Eggins, S.M., 2001. Hafnium isotope evidence for 'conservative' element mobility during subduction zone processes. *Earth and Planetary Science Letters* 192, 331–346.
- Woodhead, J.D., Hergt, J., Shelley, M., Eggins, S., Kemp, R., 2004. Zircon Hf-isotope analysis with an excimer laser, depth profiling, ablation of complex geometries, and concomitant age estimation. *Chemical Geology* 209, 121–135.
- Wu, F.Y., Sun, D.Y., Li, H.M., Jahn, B.M., Wilde, S.A., 2002. A-type granites in northeastern China: age and geochemical constraints on their petrogenesis. *Chemical Geology* 187, 143–173.
- Wu, F.Y., Yang, Y.H., Xie, L.W., Yang, J.H., Xu, P., 2006. Hf isotopic compositions of the standard zircons and baddeleyites used in U–Pb geochronology. *Chemical Geology* 234, 105–126.

- Xiao, L., Clemens, J.D., 2006. Origin of potassic (C-type) adakite magmas: experimental and field constraints. *Lithos* 95, 399–414.
- Xiao, W., Windley, B.F., Hao, J., Zhai, M., 2003. Accretion leading to collision and the Permian Solonker suture, Inner Mongolia, China: termination of the central Asian orogenic belt. *Tectonics* 22, 1069. doi:10.1029/2002TC001484.
- Yang, J.H., Wu, F.Y., Shao, J.A., Wilde, S.A., Xie, L.W., Liu, X.M., 2006. Constraints on the timing of uplift of the Yanshan fold and thrust belt, North China Craton. *Earth and Planetary Science Letters* 246, 336–352.
- Yang, Y.H., Wu, F.Y., Wilde, S.A., Liu, X.M., Zhang, Y.B., Xie, L.W., Yang, J.H., 2009. In situ perovskite Sr–Nd isotopic constraints on the petrogenesis of the Ordovician Mengyin kimberlites in the North China Craton. *Chemical Geology* 264, 24–42.
- Yang, K.F., Fan, H.R., Santosh, M., Hu, F.F., Wang, K.Y., 2011. Mesoproterozoic mafic and carbonatitic dykes from the northern margin of the North China Craton: implications for the final breakup of Columbia supercontinent. *Tectonophysics* 498, 1–10.
- Yarmolyuk, V.V., Kovalenko, V.I., Salnikova, E.B., Kovach, V.P., Kozlovsky, A.M., Kotov, A.B., Lebedev, V.I., 2008. Geochronology of igneous rocks and formation of the late Paleozoic south Mongolian active margin of the Siberian continent. *Stratigraphy and Geological Correlation* 16, 162–181.
- Yuan, B.G., Wang, H.C., 2006. Magmatic activity and its tectonic implications during the early Permian in the northwestward of Wuchuan, Inner Mongolia. *Geological Survey and Research* 29, 303–310.
- Zhang, X.H., Zhai, M.G., 2010. Magmatism and its metallogenic effects during the Paleozoic continental crustal construction in northern North China: an overview. *Acta Petrologica Sinica* 26, 1329–1341.
- Zhang, H.T., So, C.S., Yun, S.T., 1999. Regional geologic setting and metallogenesis of central Inner Mongolia, China: guides for exploration of mesothermal gold deposits. *Ore Geology Reviews* 14, 129–146.
- Zhang, Y.B., Wu, F.Y., Wilde, S.A., Zhai, M.G., Lu, X.P., 2004. Zircon U–Pb ages and tectonic implications of “Early Paleozoic” granitoids at Yanbian, Jilin Province, northeast China. *The Island Arc* 13, 484–505.
- Zhang, X.H., Su, W.J., Wang, H., 2005. Zircon SHRIMP geochronology of the Faku tectonites in the northern Liaoning Province, and its implications for the northern boundary of the North China Craton. *Acta Petrologica Sinica* 21, 135–142.
- Zhang, S.H., Zhao, Y., Song, B., Yang, Z.Y., Hu, J.M., Wu, H., 2007. Carboniferous granitic plutons from the northern margin of the North China block: implications for a Late Paleozoic active continental margin. *Journal of the Geological Society of London* 164, 451–463.
- Zhang, X.H., Zhang, H.F., Tang, Y.J., Wilde, S.A., Hu, Z.C., 2008. Geochemistry of Permian bimodal volcanic rocks from Central Inner Mongolia, North China: implication for Tectonic setting and Phanerozoic continental growth in Central Asian Orogenic Belt. *Chemical Geology* 249, 261–281.
- Zhang, S.H., Zhao, Y., Song, B., Hu, J.M., Liu, S.W., Yang, Y.H., Chen, F.K., Liu, X.M., Liu, J., 2009a. Contrasting Late Carboniferous and Late Permian–Middle Triassic intrusive suites from the northern margin of the North China Craton: geochronology, petrogenesis and tectonic implications. *Geological Society of America Bulletin* 121, 181–200.
- Zhang, S.H., Zhao, Y., Kroner, A., Liu, X.M., Xie, L.W., Chen, F.K., 2009b. Early Permian plutons from the northern North China Block: constraints on continental arc evolution and convergent margin magmatism related to the Central Asian Orogenic belt. *International Journal of Earth Sciences* 98, 1441–1467.
- Zhang, X.H., Wilde, S.A., Zhang, H.F., Tang, Y.J., Zhai, M.G., 2009c. Geochemistry of hornblende gabbros from Sonidzuoqi, Inner Mongolia, North China: implication for magmatism during the final stage of suprasubduction zone ophiolite formation. *International Geology Review* 51, 345–373.
- Zhang, S.H., Zhao, Y., Liu, X.C., Liu, D.Y., Chen, F.K., Xie, L.W., Chen, H.H., 2009d. Late Paleozoic to Early Mesozoic mafic–ultramafic complexes from the northern North China Block: constraints on the composition and evolution of the lithospheric mantle. *Lithos* 110, 229–246.
- Zhang, X.H., Zhang, H.F., Jiang, N., Zhai, M.G., Zhang, Y.B., 2010a. Early Devonian alkaline intrusive complex from the northern North China Craton: a petrologic monitor of post-collisional tectonics. *Journal of the Geological Society of London* 167, 717–730.
- Zhang, X.H., Zhang, H.F., Wilde, S.A., Yang, Y.H., Chen, H.H., 2010b. Late Permian to Early Triassic mafic to felsic intrusive rocks from North Liaoning, North China: petrogenesis and implication for Phanerozoic continental growth. *Lithos* 117, 283–306.
- Zhang, X.H., Wilde, S.A., Zhang, H.F., Zhai, M.G., 2011. Early Permian high-K calc-alkaline volcanic rocks from northwest Inner Mongolia, North China: geochemistry, origin and tectonic implications. *Journal of the Geological Society of London* 168, 525–543.
- Zhao, G.C., Wilde, S.A., Cawood, P.A., Sun, M., 2001. Archean blocks and their boundaries in the North China Craton: lithological, geochemical, structural and P–T path constraints and tectonic evolution. *Precambrian Research* 107, 45–73.
- Zhou, X.H., Sun, M., Zhang, G.H., Chen, S.H., 2002. Continental crust and lithospheric mantle interaction beneath North China: isotopic evidence from granulite xenoliths in Hannuoba, Sino–Korean Craton. *Lithos* 62, 111–124.